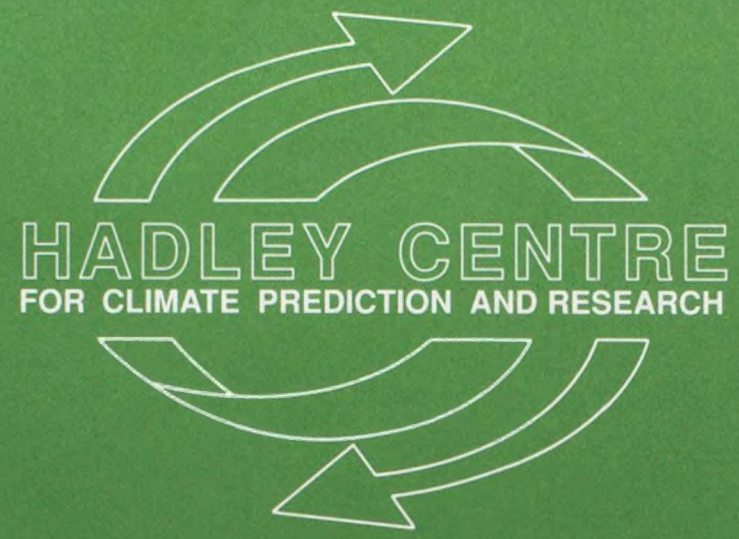

ENSO Prediction experiments using a simple ocean - atmosphere model

by

D. - H. Wu, D.L.T. Anderson and M.K. Davey

CRTN 39

July 1993

CLIMATE
RESEARCH
TECHNICAL
NOTE

Hadley Centre
Meteorological Office
London Road
Bracknell
Berkshire RG12 2SY

CLIMATE RESEARCH TECHNICAL NOTE NO. 39

ENSO PREDICTION EXPERIMENTS USING A SIMPLE OCEAN-ATMOSPHERE MODEL

by

D.-H. Wu, D.L.T. Anderson, M.K. Davey

Hadley Centre for Climate Research and Prediction
Meteorological Office
London Road
Bracknell
Berkshire RG12 2SY
U.K.

Note: This paper has not been published. Permission to quote from it should be obtained from the Director of the Hadley Centre

ENSO Prediction Experiments Using A Simple Ocean-Atmosphere Model

Deng-Hua Wu* **, David L.T. Anderson**
and Michael K. Davey***

*: (from June 1993) Dept. of Meteorology,
University of Maryland, USA

**: Atmospheric, Oceanic and Planetary Physics,
University of Oxford, England

***: Hadley Centre, Meteorological Office,
Bracknell, England

Abstract

A coupled model consisting of a reduced gravity ocean and an empirical atmosphere is developed to investigate predictability of ENSO. The empirical atmosphere is constructed by using advanced statistical techniques to reproduce the observed wind anomalies using sea surface temperature anomalies simulated by the model. The focus of this study is on detailed analysis of individual predictions, as they are more useful for understanding and improving the prediction skill than statistical scores from an ensemble of predictions.

Principal Oscillation Pattern analysis of experiments with the ocean forced by observed winds or coupled to the empirical atmosphere show that the free coupled model can maintain an interannual oscillation with a delayed oscillator mechanism very similar to that associated with ENSO events in the forced simulation.

Examination of typical ENSO events shows that the skill of the model predictions is related strongly to the mechanism responsible for ENSO variability in the model. The model can in general successfully predict an event about one year in advance, provided that the initial conditions are associated with a significant heat content anomaly (positive or negative) in the western Pacific. However, the model has little ability to predict low amplitude variability that is not related to ENSO.

Predictions based on POP analysis are also made for several ENSO events: such predictions provide information about likely ENSO phase changes, but not their amplitude. Skill is comparable to that of the dynamical coupled model.

For the purposes of this technical note, full details of the construction of the empirical atmosphere and of the POP analysis are provided in appendices.

1. Introduction

The El Niño/Southern Oscillation (ENSO) phenomenon in the tropics is an important example of large scale ocean-atmosphere interaction in climate variability. It can be regarded as an oscillation between El Niño (the warm phase) and La Niña (the cold phase). During El Niño events, anomalously warm sea surface temperatures (SST) are observed in the central-eastern Pacific with small negative SST anomalies in the west. The associated atmospheric change is a weakened Walker circulation or shift of the convective centre from the west to central Pacific, and a decrease of sea level pressure difference between Tahiti and Darwin (a measure of the Southern Oscillation).

Extensive studies have focused on the mechanisms responsible for the oscillation in the coupled system, mostly by using coupled ocean-atmosphere models with limited but essential physical processes. (Anderson and McCreary, 1985; Cane and Zebiak, 1985; Anderson and McCreary, 1986; Battisti, 1988; Hirst, 1988; Suarez and Schopf, 1988; to cite a few). The feedback between the ocean and atmosphere has been confirmed to be a key factor for the oscillation, a hypothesis proposed by Bjerknes (1969) two decades ago. Under normal conditions, the pile-up of warm water with a deep thermocline in the western Pacific, and the cold tongue with shallow thermocline in the eastern Pacific, are features maintained by the prevailing easterly winds in the equatorial region. A westerly wind anomaly, for example in the western-central Pacific, would relax the easterlies and produce downwelling Kelvin waves in the ocean with a deepened thermocline anomaly propagating eastward, leading to a warm SST anomaly in the east Pacific. This SST anomaly, in turn, affects the atmosphere by providing more atmospheric heating and hence enhancing the westerly wind to the west, producing a positive feedback in the coupled system. However, the same westerly anomaly produces upwelling Rossby waves to its west which, after reflection from the western boundary as Kelvin waves, compete with the positive feedback effects and finally turn the process to the opposite phase of the cycle. This reflection effect, known as the delayed oscillator scenario, complements Bjerknes' hypothesis by incorporating the role of ocean wave dynamics in the oscillation cycle (see review by McCreary and Anderson, 1991 and references therein).

Recently, several forecasting models have been proposed for the prediction of ENSO, ranging from purely statistical methods through intermediate coupled models to fully coupled GCMs. Latif et al (1993) have reviewed the state-of-the-art of ENSO prediction: all of the models reviewed have shown some skill in predicting ENSO events about 6–12 months in advance. For the dynamically coupled ocean-atmosphere models (Cane et al, 1986 in particular), the useful lead time of prediction can be longer than one year. The success of these model predictions comes presumably from the cyclic character of ENSO and the mechanism operating in the real coupled system and models. A coupled model with both physical ocean and atmosphere components could have higher prediction skill than a statistical model, because this type of model has the potential to capture more realistically the mechanism responsible for the interannual variation. In other words, the skill could depend strongly on how well the model could reproduce the key relations between the wind stress and SST anomalies (probably with spatial and time lag, as suggested by the delayed oscillator scenario for example). In order to reproduce such relations in the observations without invoking atmospheric dynamics, Latif and Flügel (1991) and Barnett et al (1993) have tried an alternative coupled model – a physical ocean coupled to an empirical atmosphere. The empirical atmosphere is trained by determining a statistical

relation between the observed wind and SST anomalies, which are in turn related to modeled SST anomalies by another regression matrix. There are many ways to construct such an empirical atmosphere: it is therefore of interest to try experiments based on different approaches, such as that used in this paper.

Prediction skills of ENSO have commonly been estimated by statistical features of ensemble predictions, such as the correlation between predicted and observed anomalies. Detailed examinations of individual experiments, however, are also needed to better understand and improve the prediction skill. The purpose of this paper is to describe some prediction experiments using a coupled ocean-atmosphere model, focusing on the detailed analysis of typical, individual experiments. The ocean model is a reduced gravity model with only essential physics involved. The atmosphere is an empirical model developed by using an advanced statistical technique. The paper is organized as follows. Section 2 contains a description of the model and a discussion of the empirical atmosphere. Section 3 presents results of natural interannual variability of the model. The model prediction experiments are described in section 4, followed by a comparison with a prediction scheme based on Principal Oscillation Pattern (POP) analysis in section 5. Discussion and a summary of the present study are given in section 6.

2. Coupled model description

2a. The ocean model

The ocean model used in this study consists of a linear reduced gravity model with one active layer, simulating deviations of the upper layer depth (or thermocline) and associated currents. A separate equation for SST anomalies is incorporated; the anomalies are affected by horizontal advection and upwelling as determined by the dynamic set of equations. This model is similar in many respects to that of Cane and Zebiak (1985). However, the present model is simpler in that it contains only physics essential for ENSO variability, only zonal wind stress anomalies are used, and symmetry about the equator is assumed. No seasonal information is contained in the background state, and the only nonlinear term is a cubic temperature anomaly damping. This model has previously been used to investigate external impacts on ENSO variability (Wu et al 1993), and further details of the model can be found there.

2b. The empirical atmosphere

The empirical atmosphere model used here is based on the assumption that the wind stress anomaly is a linear function of SST variation alone. To determine such a function, Latif and Flügel (1991) used local point correlations between SST and wind stress anomalies. Apparent limitations appear in this approach, because wind changes can be due to remote SST anomalies. Barnett et al (1993) constructed the function by a linear regression, over a limited equatorial domain, between coefficients of EOFs (Empirical Orthogonal Function) of observed wind stress and SST anomalies. An additional corrector was needed to convert the relation from observed SST to model SST because of model errors in simulating the observed SST. We take a slightly different approach to that of Barnett et al, in that the regression is obtained by using model SST directly. Another difference from Barnett et al is that our EOF analysis is applied only to SST anomalies

and not to thermocline perturbations.

The procedure to obtain the empirical atmosphere is as follows. The model was forced by using the observed monthly Florida State University (FSU) wind stress anomalies (Goldenberg and O'Brien, 1981) from January 1961 through January 1992. Only the zonal wind component was needed in this model because of the long wave approximation in the model formulation (see Wu et al 1993). The wind stress was detrended by the same technique used in Cane et al (1986) to remove the possible long term trend; namely, the anomaly was calculated relative to the previous four-year mean with seasonal dependence. Note that there is no seasonal cycle of the forcing or of the mean state in this model.

Having obtained model SST anomalies, we want to derive the statistical relation between anomalies of the simulated SST and the observed wind stress used as the driving force for the simulation. Full details are given in Appendix A. Simulated monthly SST anomalies T^{sim}_{mn}, with index m standing for space (M points) and n for time (N months), can be expressed by singular value decomposition as:

$$T^{sim}_{mn} = \sum_{k=1}^{N} E_{mk}\, \lambda_k\, P_{nk} \tag{1}$$

where the E_{mk} are normalised components of the kth empirical orthogonal function (EOF), λ_k contains variance information, and P_{nk} is the normalised coefficient of EOF k at time n. At any time an SST anomaly pattern T can be projected onto the EOFs to obtain coefficients

$$A_k = \sum_{m=1}^{M} E_{mk} T_m \tag{2}$$

We use L of these coefficients as predictors of wind stress anomalies τ, to obtain

$$\tau_m = \sum_{l=1}^{L} W_{ml} A_l \tag{3}$$

where the W_{ml} are components of the lth associated wind stress pattern. As described in Appendix A, the associated wind stresses are obtained from the observed stress τ^{obs} used in the simulation:

$$W_{ml} = \sum_{n=1}^{N} \tau^{obs}_{mn} P_{nl}/\lambda_l \tag{4}$$

The T^{sim} values actually used for the decomposition (1) started from January 1965, since the wind anomaly was calculated relative to the previous four-year mean.

The first few leading EOFs (arranged according to decreasing eigenvalues λ_k) explain a large fraction of the total variance of T^{sim} in the model. As we shall see shortly, the wind patterns associated with the leading EOFs represent physically significant signals of the wind, while those associated with higher modes of the EOFs are more noisy. Thus the number of EOFs to be used in the model is truncated. In practice, three EOFs were retained in the following calculations. The fraction of the total variance of T^{sim} accounted for by these three EOFs is 97.7%. Increasing the number of EOFs in the construction of

the wind anomaly did not appear to affect significantly the interannual variability of the model.

To see how well the leading EOFs could represent the variability in the model, the model was rerun by using reconstructed wind stress (3) in place of the observed wind stress to drive the ocean. The time coefficients for the associated wind patterns were taken from the decomposition (1) of the forced run using the observed wind. (I.e. $A_k = \lambda_k P_{nk}$ at timepoint n.) The forced run with the reconstructed wind started from January 1965, which is the starting point of the timeseries for the decomposition. Fig.1 shows the time evolution of SST anomalies along the equator, calculated by using the observed wind (Fig.1a) and using the reconstructed wind with three EOFs retained in (3) (Fig.1b). From Fig.1a, it can be seen that the model captures every warm/cold event during the period shown, with the amplitudes mainly confined to the central-eastern Pacific. However, the spatial structure (not shown) of the anomalies is too concentrated in the equatorial region compared with that observed. The errors due to the EOF truncation can be seen by comparing Fig.1b with Fig.1a. The peaks of the amplitude are reduced in Fig.1b; however, the overall evolution in the figures looks quite similar, demonstrating that the interannual variation could be captured by the truncated wind anomalies.

It is useful to examine the extent to which the empirical atmosphere could reflect the actual physics of the coupling between the ocean and atmosphere. This is easily done in the present case because in our approach there is a one-to-one correspondence between anomaly patterns of EOFs and associated winds. Fig.2a shows the first three EOF patterns of T^{sim} on the left and the associated wind patterns on the right. Fig.2b shows the corresponding principal components (time series) P_{nl}. Most variance is accounted for by the first EOF (87.3%) in this model. From Fig.2b, it can be seen that the PC peaks of the first EOF correspond well with ENSO events during the period (see Fig.1a). The amplitude of the first EOF pattern is confined to the central-eastern Pacific, which is very similar to the SST anomaly patterns during ENSO events as simulated in the model. The associated zonal wind pattern shows large amplitude over the west Pacific, with a maximum centered near the dateline. The meridional scale of the wind is much larger than that of SST. These are all characteristics also found in observations (Rasmusson and Carpenter, 1982; Latif et al, 1993). Moreover, the distributions of the SST and wind patterns are in the relation as suggested by the delayed oscillator scenario: a westerly wind anomaly in the central-western Pacific is associated with an SST anomaly in the central-eastern Pacific. It is worth pointing out that in the model there is no significant easterly wind associated with the EOF 1 SST anomaly. Many dynamical atmosphere models have a wind anomaly to the east of the SST anomaly, which is not present in the observations. The second and third EOFs explain much less variance of T (8.36% for the second EOF and 2.04% for the third) than does the first EOF. The associated zonal wind patterns of these modes also show a correspondence between warm/cold SST and westerly/easterly wind anomalies, indicating that the empirical atmosphere reflects realistically the coupling physics in the tropical system.

3. POP analysis and the mechanism for interannual variability

By investigating wave components, it has been shown that the delayed oscillator mechanism played a major role in generating the interannual variability in this model

when the model ocean was coupled to a dynamical atmosphere (Wu et al 1993). Here we take an alternative approach, and use POP (Principal Oscillation Pattern) analysis to examine the mechanism operative in the model.

POP analysis is a technique to identify time-dependent patterns in a set of timeseries (Hasselmann, 1988; von Storch, 1988). Details of the analysis as applied here are given in Appendix B for convenience. Suppose a dataset is decomposed into EOFs and PCs. By applying POP analysis, that data can be re-expressed as a superposition of POP spatial patterns and timeseries, where the POP patterns represent independent modes that would evolve as decaying oscillations in the absence of forcing. In the notation of Appendix B, an oscillating mode has 'real' and 'imaginary' spatial patterns $\underline{pop}_R$ and $\underline{pop}_I$, with actual timeseries of corresponding coefficients denoted $\underline{popt}_R$ and $\underline{popt}_I$, and characteristic period τ and e-folding decay time D.

If the system is dominated by one particular POP mode, then insights into the mechanism operating in the system can be obtained by examining the spatial patterns and time behaviour. To do so, measures are needed to pick out useful or significant POP modes. Apart from the obvious matching of the oscillation period τ to the interannual ENSO timescale, three indicators are used in our analysis.

1): How well the actual POP mode evolution resembles the oscillation of an unforced POP mode. This is examined by taking lag correlations between $\underline{popt}_R$ and $\underline{popt}_I$. A well-behaved POP mode will have a positive maximum correlation at a lag of $\tau/4$ with the imaginary part leading the real part. The position and amplitude of the maximum are equally relevant in this measure. In addition, the decay timescale of a POP mode is another useful measure. A significant POP mode should have an e-folding time at least comparable to its oscillation period, otherwise the POP pattern will virtually disappear before one cycle has completed according to (B9), unless forcing 'noise' is large.

2): Comparison of the variance accounted for by a particular POP mode with that of other modes. A useful POP mode should account for a significant fraction of the variance of the original data. It should be emphasized, however, that since the POP modes are not orthogonal to each other, the variance of each mode is not additive. As a consequence, a spuriously high fraction of variance may result if it was calculated by the ratio of the variance of the field constructed from one POP mode to the variance of the reconstructed data using all the POP modes, i.e. the original data. [This can be readily demonstrated by a larger-than-one ratio of total variance accounted for by all the POP modes to variance of the original data, if they non-vanishingly project onto each other.] Instead a modified fraction of variance is calculated in the present analysis: First calculate variance V_k by using the kth POP mode. Then normalization of the variance V_k by $\sum_j V_j$ (summing over all POP modes) gives a modified fraction of variance of the kth mode. This fraction of variance does not provide the same measure as in EOF analysis and tends to be small. It can be used, however, as an inter-modal comparison of relative significance.

3): Correlation of the POP coefficients with a given timeseries which may be an index of some phenomenon under consideration. For our purpose, the timeseries of SST anomalies averaged over the Niño3 region (150°W–90°W, 5°S–5°N) provides a good index for ENSO. A POP mode representing ENSO can be expected to have higher correlation with this timeseries than other (non-ENSO) modes.

Since coherent structures in the atmospheric and oceanic variables are observed during ENSO events, it is useful to examine the oscillatory patterns in these variables as a unified system. Anomalies of sea surface temperature, the upper layer depth and zonal wind stress are used in the following analysis. (Thus, matrix $\underline{\underline{Z}}$ in (B1) contains temperature, depth and wind information.) The anomalies for different variables were normalized by their respective standard deviations before being combined to form a unified dataset. EOF analysis was then applied to reduce the number of degrees of freedom. In the following, results of POP analysis applied to the forced run and a coupled run are presented; comparison of the two runs reveals how natural oscillations are maintained in the model.

3a. Forced run

For the forced run, 20 EOFs were retained for POP analysis. The fraction of total variance of the combined dataset explained by these EOFs is 91%. Sensitivity experiments showed that the number of EOFs retained in the analysis did not have a significant influence on the POPs. The spatial structures of the first three EOFs for SST and zonal wind (not shown) are fairly similar to those shown in Fig.2a, which were obtained by applying EOF analysis to the SST anomalies alone and determining the associated winds. The POP mode which best represents ENSO in the simulation has an oscillation period of 31.5 months and e-folding time of 17 months. Fig.3a shows lag correlations of the observed Nino3 SST anomaly timeseries with the timeseries of real (solid) and imaginary (dashed) POP coefficients for that mode. The dash-dotted line represents lag correlation between the real and imaginary POP coefficients. A positive maximum correlation of about 0.65 is seen at a lag time of about 8 months with the imaginary coefficient leading the real one. This implies that the phase evolution of the POP mode virtually satisfies the requirement of the theoretical model (B8). The maximum correlation of the POP coefficients with Niño3 SST anomalies is about -0.8 for the imaginary part, indicating that this POP mode is likely to be an ENSO mode. In addition, this POP mode has the largest fraction of variance (24.4%) compared to other POP modes. Together these results indicate (see the three criteria mentioned above) that this POP mode represents the dominant interannual mode in the forced simulation fairly well, and that it is related to ENSO.

Fig.3b shows the POP patterns $\underline{pop}_R$ and $\underline{pop}_I$, and Fig.3c shows the corresponding timeseries of POP coefficients, for this ENSO-like mode. As the timeseries are nearly 90°out of phase, the real and imaginary patterns in Fig.3b will be actually observed a quarter of the period apart, in the sequence $\underline{pop}_R \rightarrow (-\underline{pop}_I) \rightarrow (-\underline{pop}_R) \rightarrow \underline{pop}_I \rightarrow \underline{pop}_R$. The real temperature pattern $\underline{pop}_R$ shows a weak anomaly in the central Pacific, while the imaginary pattern $\underline{pop}_I$ has large amplitude in the central-eastern Pacific. The anomalies in temperature and layer depth are positively correlated, especially in the central-eastern equatorial Pacific: a warm event is associated with deeper thermocline in the east Pacific, and vice versa. The real pattern represents a transition phase, and the imaginary pattern corresponds to peak phase of the ENSO cycle. The big difference in the amplitudes of the real and imaginary patterns of SST anomaly (Fig.3a) suggests that the temperature anomaly is basically a standing oscillation. This is in contrast to the situation in the layer depth anomaly patterns, where the real and imaginary patterns have comparable amplitudes, suggesting propagation. In the peak phase of a cold event, large negative anomalies of the layer depth are observed in the eastern Pacific; a quarter of a period later, the negative anomalies are replaced by weak positive anomalies in the equatorial region. This can be attributed to the propagation of positive anomalies accumulated in

the western Pacific during the peak phase. In the next half cycle, the positive anomalies grow in the central-eastern Pacific and then decay due to arrival of the negative anomalies from the west. Moreover, the structures of the patterns are very similar to a combination of Kelvin and Rossby modes. Therefore, this POP oscillation has strong similarity to the delayed oscillator scenario. This is further confirmed by an examination of the zonal wind patterns in the right column of Fig.3b. During a peak phase, negative (positive) zonal wind anomalies in the central-western Pacific produce negative (positive) layer depth anomalies to the east and positive (negative) anomalies to the west, and the latter form the seed of negative feedback effects to reverse the peak, as in the delayed oscillator scenario.

Each ENSO event simulated in the model can be traced in the POP timeseries shown in Fig.3c. A warm event in peak phase is associated with a minimum of the imaginary coefficient (dashed line) for the POP mode shown in Fig.3. It is noted, however, that the POP coefficients are obtained without explicitly taking account of the characteristic timescale of the POPs (i.e. the period and e-folding time). In other words, different POP pairs may have similar time evolution regardless of their periods and e-folding timescales, as long as the pairs have similar spatial patterns. [In general, there will be no identical spatial patterns observed in different POPs, unless the matrix $\underline{\underline{B}}$ in appendix B is degenerate.] This again makes the lag correlation between the real and imaginary POP coefficients (Fig.3a, dash-dotted line) useful as an indicator of relevance to ENSO. The time lag of the positive maximum correlation is also relevant in this regard; a POP mode with a time lag quite different from a quarter of its oscillation period would be less useful (i.e. more likely to be strongly noise forced in the forced run.)

3b. Coupled run

Before carrying out the prediction experiments, the model was run in a freely coupled mode using the empirical atmosphere derived in section 2. This calculation was performed for 15 model years. An almost regular interannual oscillation was obtained and the period was about 2.5 years from an inspection of a Hovmoller diagram of SST anomalies along the equator (not shown). The maximum amplitude of the anomalies was about 2.5°C, comparable to that of the forced run. An increase of the coupling coefficient was not needed to obtain oscillations in the coupled mode in our case, in contrast to Barnett et al. (1993). Note that phase locking to the seasonal cycle cannot occur, because the model contains no seasonal information. Note also that the coupled model is symmetric in that positive and negative anomalies evolve in the same way with opposite sign.

The same POP analysis as in the forced run was applied to the output of the coupled run. In this case 10 EOFs were retained, which accounted for almost 100% of the total variance of the combined dataset. One dominant POP mode was found, whose period is about 30.6 months. The value of τ in (B9) is negative, implying a growing mode. This may result from the fact that the amplitude of the oscillation in the integration has not completely reached an equilibrium. Nevertheless, the POP analysis provides a clear picture of how the system evolves, as well as a comparison with the forced run. Fig.4a shows lag correlation of the real and imaginary timeseries of POP coefficients. The positive and negative maximum correlations (almost ± 1) are at a time lag almost exactly equal to a quarter period, implying that variability on interannual time scale in the system is dominated by this POP mode. This mode also has the largest modified fraction of variance (97.6%). Fig.4b shows spatial patterns of the mode. Comparing with Fig.3b,

the corresponding patterns are very similar to those of the forced run, although the wind has more fine structure in the forced run. (The difference can be explained to some extent by the truncation of EOFs in building up the empirical atmosphere.) Therefore the mechanism described for the forced run applies here as well. In other words, the model was able to pick up the basic mechanism operating in the forced run to maintain a natural oscillation in the coupled mode. It is of interest to note that in the coupled run, the POP coefficients are nearly regular sinusoidal oscillations by themselves (Fig.4c). This is merely an indication that the spatial patterns of this POP mode almost exactly match those of the variability which has the same time scale as the POP.

4. Prediction experiments

Prediction experiments were carried out using the same empirical atmosphere as in the coupled run described in the previous section; i.e. constructed with 3 SST EOFs. The initial conditions were taken from the run forced with FSU winds. At starting points of the predictions, errors relative to the forced run were effectively introduced into the system by the truncation of the atmospheric model to 3 associated wind patterns. These errors, however, were mostly of small scale; their impact on large scale, interannual variability remains unclear since small scale features in the atmosphere are likely to be filtered out by the ocean. The predictions were started every 3 months (January 1, April 1, July 1 and October 1); and each prediction was performed for two years. The first prediction was started in January 1965, and the last one in October 1991; so in the following analysis there are 108 prediction experiments in total. Before investigating ensemble features of the predictions, individual predictions of some typical ENSO episodes are examined in order to gain some insights into how the model captures or misses a target event. For most results presented, the predictions are compared against the forced run, which will also be referred to as the control run.

4a. Case studies

Five cases of typical warm and cold events are chosen for some detailed analysis in this subsection. They are the 72/73 and 86/87 warm events and the following cold events, and the 82/83 warm event. In each case, five (except four in Fig.5) predictions starting from different initial conditions are examined. Starting times of the prediction experiments selected for case studies shown in Fig.5 and Fig.6 are listed in Table 1. The 74/75 'non-event' is also included for some comment. This choice of events is motivated by the earlier study by Latif et al (1993) and by a TOGA-NEG intercomparison.

Fig.5a shows the time evolution of SST anomalies in the Niño3 region of the control run (solid lines) and 20 predictions (broken lines) for the 5 cases. The predictions, in general, follow the control run fairly well, except for the 86/87 warm event in which predictions starting in April and July 1986 diverged from the control run soon after the start. For the 72/73 warm event, each prediction was able to catch the event, but the phase changes from negative to positive were seen about 4 months later than in the control run for predictions starting in October 71 and January 72. This is related to the mechanism of generating and predicting an event in the model, as we shall see shortly. The correlations as a function of lead time between these 20 predictions and the control run (solid line) and the observations (dashed line) are shown in Fig.5b. Using the control run, the correlation drops rapidly in the first 5 months, followed by a plateau above 0.8 up to lead time of about 15 months.

At 0 lead time there is a correlation of about 0.7 between the simulation (control) run and the observations for these 20 cases. The predictions also have good correlation with the observations, as in the case when compared with the control run. All these imply useful predictions of more than one year in advance, at least as far as events are concerned.

The 74/75 'non-event' is shown in the right bottom corner of Fig.5a. In the observations, there seemed to be an incipient ENSO in the middle of 74, but it aborted later in 74. Many coupled models, however, fail to reproduce this behaviour in hindcast experiments and instead predict a warm event (according to information collected as part of a TOGA-NEG hindcast intercomparison). The present model was also unable to follow the control run, and produced a spurious warm event for predictions starting in January, April, and July 74.

To examine more details of the individual predictions and their average features for prediction of an event, Fig.6a shows the time evolution of SST anomalies along the equator for five predictions starting from different initial conditions for the 82/83 event. Fig.6b shows the anomalies of the control run (left) and the average of the 5 predictions (right). As can be seen from Fig.5a, the 82/83 case is predicted rather well. Each prediction, starting as early as July 81 or as late as July 82, was able to produce a warm event initiated in late 82 and decaying around the end of 83. The peaks of the event in each prediction were at approximately the same time. For example, for the prediction starting in July 81 a warm event was not initiated until late 82 and the maximum amplitude was around March 83; while in the prediction starting in July 82, a warm phase began to develop soon after the start of the prediction and the peak amplitude was seen around April 83. As in the control run, the largest amplitudes of the anomalies are confined to the central-eastern Pacific. The average of these predictions shows a very similar time evolution to that of the control run (see Fig.6b). The amplitude is, however, smaller in the averaged predictions than in the simulation.

Similar diagrams for the 86/87 warm event (which was the least well hindcast according to Fig.5a) are shown in Fig.7. In this case, predictions starting from different initial conditions diverged considerably. For the prediction started in January 86, a warm event soon developed, which was not seen in the control run until the end of 86 (Fig.7b), although there was some overlap in time of the warm phase between the prediction and the control run. Predictions starting in April and July 86 developed oscillations which have little similarity to the control run. Probably the best result for this case is the prediction starting in January 87, when the warm event was already underway. The time averaged evolution of the 5 predictions, nevertheless, shows somewhat similar features to that of the control run; i.e. a warm event began to develop in late 86, but lasted too long compared to the control run.

Fig.6 and Fig.7 contain typical examples of successful and unsuccessful predictions using the present model. To understand why the model prediction behaves so differently from one event to another, we examine how the model evolves from a given initial condition. For this purpose, the coefficients A_k for the EOF projections and the associated wind anomalies (see equns. 2 and 3) are analyzed. The reason for using these coefficients is twofold. First, if a prediction were perfect, then its A_k would follow closely the timeseries for the forced run; the errors would be entirely due to the truncation of EOFs retained in the coupled integration. Therefore evolution of A_k associated with each EOF provides another measure of the model prediction. Moreover, since the largest amount of the

variance of SST anomalies in the present model is associated with the first EOF which has amplitudes confined to the central-eastern Pacific (Fig.2a), the timeseries of A_1 alone closely represents a warm or cold event and its evolution. The second reason, which is more relevant for the present purpose, is that the A_k represent active links between the ocean and atmosphere in our approach. They are not only the projections of SST anomalies onto the EOFs, but also the strength of the corresponding wind anomalies. Cold SST anomalies in the central Pacific imply negative A_1, for example, which implies an easterly wind anomaly in the central-western Pacific and hence an accumulation of water in the west Pacific, which normally has negative feedbacks on A_1 through the ocean dynamics and thermodynamics.

Fig.8a shows the time evolution of A_k for the first 3 EOFs for the 82/83 event. Solid lines are the values from the control run and broken lines are the A_k values corresponding to the predictions shown in Fig.6a. Note the different amplitude scales for the first EOF (bottom) and the second (middle) and third (top) EOFs. It is seen that this event was dominated by the first EOF, and that variations with shorter time scales were present in the second and third EOFs. The predictions closely followed the general trend of the control run in the first EOF, but not in the higher modes, implying that the accuracy of the model prediction depends strongly on the first EOF. The phases of predicted A_1 for the first EOF correspond very well to those of the SST anomalies along the equator shown in Fig.6a.

Corresponding plots for the 86/87 event are shown in Fig.8b. In this case, the predicted A_k did not follow the control run very well, except for one experiment starting in January 87 which did trace the temporal evolution of the first EOF. Comparing with Fig.8a, it is noted that 4 out of 5 predictions of the 86/87 event were started with very small A_1, which would be associated with very weak wind anomalies. In other words, at the starting points, the system was in a state of weak wind and temperature anomalies; it had to evolve further to let the anomalies grow toward positive or negative phase, constrained by the mechanism of natural oscillation in the model. In fact, the coefficients A_2 of the second EOF at the starting points of April, July and October 1986 had comparable amplitudes to that of the first EOF; the growing phases were presumably determined by the combination of the two EOFs. [Recall that the wind patterns associated with the first two EOFs have similar spatial structures, see Fig.2a].

By contrast, predictions for the 82/83 event were started with considerable amplitude of the dominant A_1, indicating that the system had experienced preconditioning. (Note that, according to the structure of the ENSO mode revealed by POP analysis (see Fig.3b), large amplitude of A_1 is usually associated with large heat content anomalies in the west Pacific.) For the 82/83 event, easterly wind anomalies associated with negative A_1, for example before January 82, had piled up positive layer depth anomalies (associated with warm water) in the western Pacific, which, after reflection from the western boundary, tend to switch off the negative phase of A_1 according to the delayed oscillator scenario. In this theory, the time needed to switch A_1 from one phase to another is determined by the amount of accumulated water which is roughly proportional to the strength of the wind anomalies and hence of A_1 at the start. This seems to explain why it took longer to switch A_1 from negative to positive for the July 81 prediction than for the October 81 prediction, since the magnitude of A_1 in the former was smaller than in the latter. The amplitude of A_1, therefore, contains important preconditioning information. When it is small, higher EOF modes may play comparable roles to that of the first EOF; the system

is then not well preconditioned since there is no significant accumulation of water in the equatorial west Pacific, but the small anomalies are going to develop in the freely coupled mode because of the coupled instability. A considerable amplitude of A_1, on the other hand, indicates that the system has experienced preconditioning by accumulating warm or cold water in the west Pacific, which normally has negative feedback effects on A_1, i.e. the system is able to change phase when released from the forced run. It appears that the 86/87 event was not well preconditioned in the model, and the coefficient A_1 associated with the dominant, first EOF remained near zero during much of 1986.

To further explore the dependence of the prediction on the initial conditions, another example is shown in Fig.8c for the 72/73 warm event. When a prediction was started in July 71, a warm event was obtained, whose peak phase occurred about 4 months earlier than in the control run. This is presumably because, at the starting time, the system was about to change phase from negative to positive, indicated by significant negative A_1. It is noted that predictions starting October 71 and January 72 underwent almost identical evolution (see Fig.5a); both developed a warm event about 4 months later than in the control run. For the case of October 71, the wind anomaly associated with the first EOF was initially about zero, i.e. $A_1 \approx 0$, and the system evolved as a negative phase growth by the second EOF contribution to the wind anomaly. In the case of January 72, on the other hand, the system was about to change phase from negative to positive at the start. The almost identical evolution was merely a result of coincidence of two trajectories starting from different phases in the delayed oscillator cycle.

The dependence of the model prediction behavior on the initial amplitude of the first EOF projection A_1 is examined by calculating the prediction errors as a function of the initial value of A_1 (denoted A_{1t_0}) and of the lead time of predictions. The prediction error is defined as the difference between the Niño3 SST anomalies of the prediction and the control run, and the first 100 prediction sets are used for this calculation. Fig. 9a shows how individual errors depend on A_{1t_0} at lead times of 3, 6, and 9 months, while in Fig. 9b the errors are grouped according to the initial value A_{1t_0} in specified bands (centred on -0.8+0.15i, i=1...11), and rms errors for each band are plotted. It is seen from Fig.9 that the error grows as the lead time increases for lead time up to about 5 months, with little dependence on A_{1t_0} at first. It is of interest to note that, for lead time from about 3 to 7 months, the errors tend to be smaller for larger amplitude of A_{1t_0} (positive or negative) than for smaller A_{1t_0}. This is consistent with the case studies of the 82/83 and 86/87 events. In other words, for initial conditions with considerable amplitude of A_{1t_0}, the model is more likely to be able to catch the evolution of the control run.

Before leaving the discussion of the predictions, we present, in Fig.10, 5 forecast experiments for 93/94. A recovery of the decaying warm SST anomaly of the 91/92 event was observed, starting in April 93 (Climate Diagnostic Bulletin, 1993). The initial conditions were obtained by forcing the model using the observed wind stress anomalies. The wind stress was detrended in the usual way by calculating the anomalies relative to the previous four-year mean average. 4 of 5 forecasts showed a consistent decay of the warm anomaly, but the latest forecast, starting in March 93, stays in the warm phase until about Feb. 94. At the time of writing (May 93) it remains to be seen whether this is a good forecast or not.

The discussion of preconditioning has been based on the fact that the accumulation of positive layer depth anomalies or warm water in the western Pacific is associated with

negative zonal wind anomalies in the central-western Pacific, and vice versa. It is, therefore, worthwhile investigating the roles of the layer depth anomalies, or equivalently heat content anomalies in the present model, in communicating with the atmosphere. An alternative empirical atmosphere was constructed by using the heat content anomaly in place of the SST anomaly as a predictor for the wind anomaly in (1)–(4). The first 3 heat content EOF patterns and associated wind patterns are shown in Fig.11. The first EOF pattern, which accounts for 71% of the total variance, has an east-west dipole structure; negative anomalies in the east are accompanied by positive ones in the west, and vice versa. The associated zonal wind anomalies have large amplitudes in the central-western Pacific as in the case when the SST anomaly is used as the predictor; negative anomalies correspond to a piling up of warm water in the western Pacific. The wind pattern associated with heat content EOF1 is very similar to that associated with SST EOF1 in Fig. 2a, which indicates that the timeseries of coefficients of these two EOFs are similar.

Coupled experiments were carried out in which 3 EOFs were retained as before. In contrast to the atmosphere model with SST EOFs, no oscillatory solutions were obtained; the system reached an equilibrium state after adjustment of the initial perturbations. Thus the coupled instability can be substantially altered in this model by relating the wind directly to the heat content, rather than SST, anomaly. However, Latif and Graham (1992) have demonstrated that the heat content itself can be a useful predictor of SST anomalies. Ways of incorporating this information into a scheme to get better predictions are under investigation.

4b. Ensemble features

In the case studies in section 4a, we have shown that the model with an SST-based atmosphere can do a good job of predicting ENSOs when there is well defined preconditioning. In a quiet period of weak anomalies in the wind and SST, however, prediction using this model is less reliable. This is probably a common feature for all the existing coupled models used for ENSO prediction, although more sophisticated models like a GCM can in principle use more detailed physics to maintain a quiet evolution as in the real world. In this subsection, the ensemble features of the first 100 hindcast experiments are presented, in order to get an overall estimate of the skill of the model prediction, including both events and quiet periods.

The prediction skill is measured by the correlation between the predictions and predictand, and the corresponding root mean square (rms) error. Correlations of Niño3 and Niño4 (160°W–150°E, 5°S–5°N) SST anomalies of the predictions and control run as a function of lead time are calculated, together with the corresponding rms errors. The rms error is normalized by the standard deviation of the predictand, i.e. SST anomalies of the control run or observations. Fig.12a shows the correlations and rms errors for the Niño3 region, for predictions compared to the control run. The solid line is for the full prediction experiments, i.e. all 100 datasets are used in the calculation. The broken lines are obtained from four subgroups of the predictions. In each subgroup, the predictions were started from the same month of the year, so the four broken lines are for January, April, July and October predictions. It is seen that the correlation for the full dataset is above 0.5 up to a lead time of about 7 months. There are variations between the seasons, but they are not as large as the variations reported for models with explicit seasonal dependence in the mean state, confirming that the seasonal dependence of the prediction

skill results mainly from the seasonally-varying basic state. The rms errors show a sharp growth for lead times up to about 9 months, after which the errors tend to saturate. By a lead time of 7 months, the rms errors have reached the level of the standard deviation of the control run, which may be considered as an upper limit of a useful prediction as far as the amplitude is concerned. Comparing Fig.12a with the correlation found for the selected ENSO events in Fig.5b indicates that the correlation calculated for the full dataset has large detrimental contributions from the quiet periods of weak anomalies, which the model could not predict very well. For comparison, the correlation is also shown between the predicted and the observed SST anomalies in the Niño3 region (Fig.12b). The model errors relative to the observations in the forced simulation are indicated by the correlation at 0 lead time, which is about 0.75. The drop in the correlation as a function of lead time is similar to that for the comparison against the control run, except in the first 3 months. The rms errors, on the other hand, show a linear increase as a function of lead time, and the error reaches the standard deviation at a lead time of about 12 months for the full dataset.

Fig.13 shows the correlations and rms errors for the Niño4 region, which is in the equatorial west Pacific. The correlations stay above 0.5 against the control run up to a lead time of about 6 months (Fig.13a), but the saturation time of the rms errors is earlier than in the Niño3 region: by a lead time of about 5 months, the normalized rms errors have already reached unity. When the predictions are compared with observations, the correlation is below 0.5 except for the first couple of months (Fig.13b). The rms errors have no obvious saturation point. Clearly the predictive skill of the model is substantially lower for the Niño4 region than for Niño3.

5. Comparison with a POP prediction scheme

As mentioned in the introduction, a number of models have been suggested for ENSO prediction. The prediction scheme based on POP modes proposed by Xu and von Storch (1991) is worth some comment and comparison, regarding the relation between the prediction skill and mechanism of interannual variability. As demonstrated in section 3, POP analysis seeks to pick up dominant oscillatory mode(s) that are often associated with physically-meaningful spatial patterns reflecting mechanisms involved in the oscillation. The prediction method based on a single POP mode is to first specify an initial location for the mode in the real vs. imaginary amplitude space according to the control run, and then to follow the free trajectory in that space according to equ. B9. As can be seen from B9, the trajectory is unable to provide useful information about the future amplitude of the evolution; when $D > 0$ (as in the present case) the trajectory will always spiral toward the origin in the absence of some forcing. Nevertheless, one can concentrate on the phase determined by the mode, under the assumption that the desired exciting forcing is always present in the system to keep the mode energetic. The problem is thus reduced to identifying the location of a given initial state on the POP cycle. Note that the ENSO-related POP mode used for the following predictions was that obtained by analyzing the combined dataset of SST, layer depth and zonal wind stress anomalies (section 3). Thus the POP prediction uses initial SST, depth and wind information.

The dial plot in Fig.14 shows the evolution of the control run (solid lines with black dots) and POP predictions (broken lines) for the 5 selected cases (see Figs.5, 6 and 7

presented in section 4), with amplitudes of the real and imaginary POP patterns as axes. In general the evolutions show a clockwise rotation around the origin for the control run; the peak phase can be estimated as being when a trajectory crosses negative (positive) maximum imaginary values for a warm (cold) event (see the spatial patterns in Fig.3b). The predictions start at initial conditions 3 months apart, as for the dynamical model, and the decay factor of the amplitude in equ. B9 has been excluded from the plotting for reasons mentioned before. The blank circles on the prediction lines mark the time when the peak phase was reached in the control run, so a good prediction would have the circles located close to the negative (warm event) or positive (cold event) imaginary axis. It is seen that many of the predictions match the control run fairly well, except for the case of the 88/89 cold event (bottom right panel of Fig.14) in which all the predictions reached the peak phase about 6 months earlier than the control run. For the 72/73 warm event (top left panel), the prediction starting in July 71 reached the peak phase about 4 months earlier than the control run, as also observed in the dynamical model prediction. The 82/83 warm event shows up again as a successful prediction; all the circles are located close to the negative imaginary axis. It is of interest to note that in the case of POP prediction, 3 out of the 5 predictions for the 86/87 warm event (bottom left panel of Fig.14) are in fair agreement with the control run, in contrast to the dynamical model predictions which were all unsuccessful.

The actual time evolution of SST anomalies along the equator reconstructed and predicted using the POP mode are shown in Fig.15 for the 82/83 warm event. Fig.15a shows the anomalies represented by the control POP mode (i.e. from POP analysis of the control run, right) in comparison with actual anomalies from the control run (left). The POP mode captured the event very well, although the amplitude was reduced in the reconstruction. This realization constituted the initial conditions for the predictions shown in Fig.15b. The pattern of the POP prediction is always the same; the phase depends on the initial conditions. As mentioned before, the amplitude of the predictions should be considered as arbitrary, though they are scaled such that intercomparison within the 5 predictions can be made. As was seen in the harmonic dial plots, the predictions produced a consistent warm event with peak phase around the spring of 83. Comparing with Fig.6, it is seen that for this particular case, the POP prediction gave very similar evolution to that predicted by the dynamical model.

The 86/87 warm event, however, points out the difference between the two schemes: the POP scheme did a better job than the dynamical model for predictions starting in April, July and October 86 (compare Fig.16b and Fig.7a). The difference arises because the two schemes concentrate on different elements of the ENSO mechanism. Both schemes are able to identify the amplitude and location of an initial state in the cycle of the natural oscillation of the model. While the dynamical scheme traces the evolution by the amplitude and phase, the POP scheme captures only the cyclic character, leaving the amplitude undetermined. In other words, the POP prediction scheme picks up only the phase configuration of the patterns (Fig.3b) at the start, and the evolution afterwards is independent of the amplitude of the initial configuration. However, using the same configuration as the initial condition, the evolution of the dynamical prediction scheme (which is amplitude dependent) could be growth or decay, and the oscillation character could also depend on the amplitude.

Finally, we show the SST anomalies along the equator reconstructed (Fig. 17a) and predicted (Fig. 17b) using the POP mode, together with the control run, for the 88/89

cold event. This is an example in which the dial plot (Fig.14) did not show promising predictions. The cold phase lasted for more than two years in the control run (Fig.17a), which was much longer than half the period of the POP mode. The long-lasting behavior was manifested in the dial plot by the concentration of many black dots in the upper-left quadrant. The reconstruction of the cold event using the POP mode was in good agreement with the control run. However, the POP predictions necessarily oscillate with their natural 30 month period, and cannot capture the long cold phase.

6. Discussion and summary

In order to gain better understanding of the predictability of ENSO in coupled ocean-atmosphere models, we have focused on a detailed analysis of model predictions in a simple coupled system. The ocean component used consists of a one-and-half layer, reduced gravity model. The empirical atmosphere is constructed by using an advanced statistical technique to relate the observed wind anomalies to the model-simulated SST anomalies. The results show that the empirical atmosphere could capture the basic atmospheric response to SST anomalies, particularly on ENSO time scales as demonstrated in the coupled run in section 3. The main purpose of this study was to examine how the model catches or misses a target event. This is probably a necessary approach to understand and to provide hints on how to improve the prediction skill.

The case studies show that the ability of the model to predict an event was best when it could identify preconditioned information in the initial conditions. It seemed more difficult for the model to follow a quiet evolution of weak anomalies in the wind and SST. This behavior can be explained by the mechanism responsible for the interannual variations in the model. When the prediction is started, the system is released from the forced mode to a free evolution determined by the natural oscillation mechanism of the model. At the start of a prediction, it is necessary for the model to identify where the given initial condition is on the trajectories of its own natural oscillation cycle. For initial conditions with well preconditioned information, i.e. large amplitude of A_{1t_0} in our model, the trajectory of the prediction is more likely to match that of the evolution observed in the control run, since the system in the coupled mode could pick up essentially the same mechanism that is responsible for the variations on this time scale. A mismatch of the trajectories of the prediction and control, on the other hand, indicates that the evolution of the control may not be due to the same mechanism as that which the prediction model has picked up. This is probably true in the present model, as the mismatches were observed mostly during quiet periods in which the variations had small amplitudes and shorter time scales that were likely caused by effects other than the ENSO mechanism.

A comparison was made between the dynamical model prediction and the POP prediction scheme proposed by Xu and von Storch (1991). It was shown that the prediction skills of both schemes come from their ability to capture, at least partly, the mechanism of the ENSO cycle. While the dynamical model could identify both amplitude and phase of an initial condition in the natural oscillation cycle, the POP scheme only needed the phase information from the initial condition and gave no amplitude estimation for the future evolution. Both schemes showed, in general, comparable skills for prediction of the events, although differences were observed for individual predictions. It should be pointed out that the POP analysis was carried out by using the combined dataset; so the POP

scheme contains information not only of SST, but also of heat content anomalies. It would be of interest to examine the prediction skill of the dynamically coupled model when heat content information is included in the prediction scheme.

In summary, the results presented in this paper show that predictability of ENSO in a coupled model depends strongly on the mechanism responsible for variations on ENSO time-scales in the model. While statistical features such as correlation and rms error provide an overall estimate of the model's predictive capability, detailed analysis of individual predictions is equally beneficial, and useful for understanding and improving the prediction skill. Examination of individual predictions by the coupled model shows that as the model contains the essential physics for the ENSO mode, it can predict an ENSO event provided that the initial conditions are well preconditioned. But it can also produce spurious events at other times by the same mechanism for ENSO variability.

Another important effect on the predictive skill is the inevitable errors in the initial conditions, which could be responsible for the quick drop in the correlations during the first few months of lead time (Figs.5, 12, and 13). Goswami and Shukla (1992) and Blumenthal (1991) have discussed this issue from different approaches. We have instead concentrated on the long term behaviour of the predictions in this study. A thorough investigation of the model prediction skill of ENSO, however, should include both the short term (first few months) and long term behaviour, and will be the subject of further work.

Acknowledgement: The authors wish to thank M.R. Allen and M.A. Balmaseda for their substantial assistance with the statistical techniques used in the study. This work was partly supported by the NERC through grant GR3-7366.

References

Anderson, D.L.T. and J.P. McCreary, 1985a: Slowly propagating disturances in a coupled ocean-atmosphere model. *J Atmos Sci*, **42**, 615–629.

Anderson, D.L.T. and J.P. McCreary, 1985b: On the role of the Indian Ocean in a coupled ocean-atmosphere model of El Niño and the Southern Oscillation. *J Atmos Sci*, **42**, 2439–2442.

Barnett, T.P., M. Latif, N. Graham, M. Flügel, S. Pazan, and W. White, 1993: ENSO and ENSO related predictability, Part 1: Prediction of equatorial sea surface temperature with a hybrid coupled ocean-atmosphere model. *J Clim*, submitted.

Battisti, D.S., 1988: Dynamics and thermodynamics of a warming event in a coupled tropical atmosphere-ocean model. *J Atmos Sci*, **45**, 2889–2919.

Bjerknes, J., 1969: Atmospheric teleconnections from the equatorial Pacific. *Mon Weath Rev*, **97**, 163–172.

Blumenthal, M.B., 1991: Predictability of a coupled ocean-atmosphere model. *J Clim*, **4**, 766–784.

Cane, M.A. and S.E. Zebiak, 1985: A theory for El Niño and the Southern Oscillation. *Science*, **228**, 1085–1087.

Climate Diagnostics Bulletin, May 1993. CAC, US Department of Commerce

Goldenberg,S.D. and J.J. O'Brien, 1981: Time and space variability of tropical Pacific wind stress. *Mon Weath Rev*, **109**, 1190–1207.

Goswami, N.E. and J. Shukla, 1991: Predictability of a coupled ocean-atmosphere model. *J Clim*, **4**, 3–22.

Hasselmann, K., 1988: PIPs and POPs: The reduction of complex dynamical systems using Principal Interaction and Oscillation Patterns. *J Geophys Res*, **93**(D9), 11015–11021.

Hirst, A.C., 1988: Slow instabilities in tropical ocean basin-global atmosphere models. *J Atmos Sci*, **45**, 830–852.

Latif, M. and M. Flügel, 1991: An investigation of short range climate predictability in the tropical Pacific. *J Geophys Res*, **96**(C2), 2661–2673.

Latif, M. and N.E. Graham, 1992: How much predictive skill is contained in the thermal structure of an oceanic GCM ? *J Phys Oceanog.* **22**, 951–962.

Latif, M., T.P. Barnett, M.A. Cane, M. Flügel, N.E. Graham, H. von Storch, J.-S. Xu and S.E. Zebiak, 1993: A review on ENSO prediction studies. *Climate Dyn*, submitted.

Latif, M., T.P. Barnett and K. Mizuno, 1993: Model structure of variations in the tropical climate system. submitted to *J Atmos Sci.*

McCreary, J.P. and D.L.T. Anderson, 1991: An overview of coupled ocean-atmosphere models of El Niño and the Southern Oscillation. *J Geophys Res*, **96**, 3125–3150.

Press, W.H., Flannery, B.P., Teukolsky, S.A. and W.T. Vetterling, 1986: Numerical Recipes. Cam. Univ. Press, 818pp.

Rasmusson, E.M. and T.H. Carpenter, 1982: Variations in tropical sea surface temperature and surface wind fields associated with the Southern Oscillation/El Niño. *Mon Weath Rev*, **110**, 354–384.

Suarez, M.J. and P.S. Schopf, 1988: A delayed action oscillator for ENSO. *J Atmos Sci*, **45**, 3283–3287.

von Storch, H., T. Bruns, I. Fischer-Bruns and K. Hasselmann, 1988: Principal oscillation analysis of the 30 to 60 day oscillation in a GCM. *J Geophys Res*, **93**(D9), 11022–11-36.

Wu, D.-H., D.L.T. Anderson and M.K. Davey, 1993: ENSO variability and external impacts. *J Clim*, in press.

Xu, J.-S. and H. von Storch, 1990: Principal oscillation patterns–prediction of the state of ENSO. *J Clim*, **3**, 1316–1329.

Appendix A Construction of an empirical atmosphere model

We seek an empirical atmosphere model that will provide a surface wind stress anomaly spatial pattern as output when given a sea surface temperature anomaly spatial pattern as input. There are many ways of constructing such a model: one method is described here. The zonal wind stress component is considered here; a similar procedure can be used independently for the meridional component if required.

Suppose the observed zonal wind stress anomaly pattern is the $M_a \times N$ matrix

$$\underline{\underline{\tau}}^{obs} = \begin{bmatrix} \tau_{11}^{obs} & \cdots & \tau_{1N}^{obs} \\ \vdots & \vdots & \vdots \\ \vdots & \vdots & \vdots \\ \vdots & \vdots & \vdots \\ \tau_{M_a1}^{obs} & \cdots & \tau_{M_aN}^{obs} \end{bmatrix} \qquad (A1)$$

for M_a spatial points and N time points. The spatial points refer to a latitude-longitude grid ordered in some prescribed way, so a column of $\underline{\underline{\tau}}^{obs}$ corresponds to a spatial pattern (denoted $\underline{\tau}^{obs}$) at a fixed time. A row of $\underline{\underline{\tau}}^{obs}$ corresponds to a time series at a fixed point.

This wind stress anomaly pattern is used to force an ocean model, to obtain an $M \times N$ matrix of model simulated sea surface temperature anomalies

$$\underline{\underline{T}}^{sim} = \begin{bmatrix} T_{11}^{sim} & \cdots & T_{1N}^{sim} \\ \vdots & \vdots & \vdots \\ \vdots & \vdots & \vdots \\ \vdots & \vdots & \vdots \\ T_{M1}^{sim} & \cdots & T_{MN}^{sim} \end{bmatrix} \qquad (A2)$$

for a grid of M spatial points (not necessarily the same grid as for the wind stress: M need not be equal to M_a) and the same N time points. Anomalies at any land points where SST is undefined are set to zero, so matrix rows (timeseries) at such points are zero. Generally mean values are removed at each spatial point in calculating anomalies, so, for all m, $\sum_{n=1}^{N} T_{mn}^{sim} = 0$.

Given this information, the aim is to find a way of estimating the stress anomaly spatial pattern $\underline{\tau}$ at some instant, given the temperature anomaly spatial pattern $\underline{T}$ at that time. The general approach is to use $\underline{T}$ to calculate L predictors $A_1 \ldots A_L$, then to use wind stress patterns associated with the predictors to find $\underline{\tau}$, as described in section A1 below. In particular, Singular Value Decomposition (SVD) is applied to $\underline{\underline{T}}^{sim}$ to find temperature anomaly empirical orthogonal functions and timeseries as described in section A2. This information can then be used to construct an empirical atmosphere,

as in section A3. Note: although $\underline{T}$ is specifically referred to as SST anomalies here, the same method can be applied using other ocean fields, such as heat content, or combinations of fields.

A1. General principles

We wish to estimate the stress pattern $\underline{\tau}$ as

$$\underline{\tau} = [\underline{w}_1 \ \cdots \ \underline{w}_L] \begin{bmatrix} A_1 \\ \vdots \\ A_L \end{bmatrix} = \underline{\underline{W}} \ \underline{\underline{A}} \qquad (A3)$$

using SST-based predictors A_l, and associated wind stress spatial patterns $\underline{w}_l$ which need to be determined. Suppose that for time points 1 to N the predictors calculated using $\underline{\underline{T}}^{sim}$ form the known $L \times N$ matrix $\underline{\underline{A}}$. Then the estimated wind stress anomalies for these times are

$$\underline{\underline{\tau}}^{est} = \underline{\underline{W}} \ \underline{\underline{A}} \qquad (A4)$$

The patterns $\underline{\underline{W}}$ can be determined by requiring a least squares fit between estimated values $\underline{\underline{\tau}}^{est}$ and the known values $\underline{\underline{\tau}}^{obs}$. Minimising

$$\sum_{m=1}^{M_a} \sum_{n=1}^{N} (\tau_{mn}^{est} - \tau_{mn}^{obs})^2 \qquad (A5)$$

leads to

$$\underline{\underline{W}} = (\underline{\underline{\tau}}^{obs} \ \underline{\underline{A}}^T) \ (\underline{\underline{A}} \ \underline{\underline{A}}^T)^{-1} \qquad (A6)$$

where superscript T denotes a transpose. (See e.g. Press et al. (1986) section 14.3 for details, and for robust ways of calculating $\underline{\underline{W}}$ in general.)

We need to choose suitable predictors. Why not just use all the grid point values of $\underline{T}$ as the predictors? A large number of predictors would be cumbersome, and contain a lot of noise to mislead the prediction. Typically we want to use just a few predictors that represent the robust major features of the system.

A2. Singular Value Decomposition

One way (not physically based) of finding these major features is to use empirical orthogonal functions. Singular Value Decomposition (SVD) is a numerical algorithm that can be used to write $\underline{\underline{T}}^{sim}$ in the form

$$\underline{\underline{T}}^{sim} = [\underline{eof}_1 \ \cdots \ \underline{eof}_N] \begin{bmatrix} \lambda_1 & 0 & 0 \\ 0 & \ddots & 0 \\ 0 & 0 & \lambda_N \end{bmatrix} \begin{bmatrix} \underline{pc}_1^T \\ \vdots \\ \underline{pc}_N^T \end{bmatrix} \qquad (A7)$$

In scalar form,

$$T^{sim}_{mn} = \sum_{k=1}^{N} E_{mk}\ \lambda_k\ P_{nk}$$

(Note: we have assumed $M > N$.) Each vector $\underline{eof}_k$ is a spatial pattern (empirical orthogonal function EOF) with M values E_{mk}. Each $\underline{pc}_k$ is a timeseries (principal component PC) of coefficients P_{nk} at timepoints $n = 1...N$ for the corresponding $\underline{eof}_k$. The EOFs are orthonormal, as are the PCs: for $k = 1...N$,

$$\underline{eof}_k^T\ \underline{eof}_k = \sum_{m=1}^{M} E^2_{mk} = 1 \qquad (A8)$$

$$\underline{pc}_k^T\ \underline{pc}_k = \sum_{n=1}^{N} P^2_{nk} = 1$$

The λ_n contain variance information, such that

$$Var(\underline{\underline{T}}^{sim}) = \sum_{m=1}^{M}\sum_{n=1}^{N} T^{sim\ 2}_{mn} = \sum_{n=1}^{N} \lambda_n^2 \qquad (A9)$$

and the fraction of total variance associated with $\underline{eof}_k$ is

$$\lambda_k^2\ /\ \sum_{n=1}^{N} \lambda_n^2 \qquad (A10)$$

A3. Empirical atmosphere from EOFs etc.

We will use $L < N$ of these EOF patterns and timeseries (typically choosing those corresponding to largest λ). Denote these subsets by

$$\underline{\underline{E}} = [\underline{eof}_1\ \ \cdots\ \ \underline{eof}_L],\ \underline{\underline{\Lambda}} = \begin{bmatrix} \lambda_1 & 0 & 0 \\ 0 & \ddots & 0 \\ 0 & 0 & \lambda_L \end{bmatrix},\ \underline{\underline{P}} = [\underline{pc}_1\ \ \cdots\ \ \underline{pc}_L] \qquad (A11)$$

Note that from the orthonormal properties (A8)

$$\underline{\underline{E}}^T\ \underline{\underline{E}} = \underline{\underline{I}} = \underline{\underline{P}}^T\ \underline{\underline{P}} \qquad (A12)$$

and that

$$\underline{\underline{P}}^T = \underline{\underline{\Lambda}}^{-1}\ \underline{\underline{E}}^T\ \underline{\underline{T}}^{sim} \qquad (A13)$$

where

$$\underline{\underline{\Lambda}}^{-1} = \begin{bmatrix} 1/\lambda_1 & 0 & 0 \\ 0 & \ddots & 0 \\ 0 & 0 & 1/\lambda_L \end{bmatrix}$$

We choose the predictors $\underline{A}$ to be the coefficients obtained by multiplying the SST anomaly $\underline{T}$ at any instant by the selected EOF patterns:

$$\underline{A} = \underline{\underline{E}}^T \, \underline{T} \qquad (A14)$$

i.e.

$$A_l = \sum_{m=1}^{M} E_{ml} \, T_m$$

For times 1 to N, using $\underline{\underline{T}}^{sim}$ and applying (A13), these predictors lead to the matrix

$$\underline{\underline{A}} = \underline{\underline{E}}^T \, \underline{\underline{T}}^{sim} = \underline{\underline{\Lambda}} \, \underline{\underline{P}}^T \qquad (A15)$$

Hence $\underline{\underline{A}} \, \underline{\underline{A}}^T = \underline{\underline{\Lambda}}^2$ (using (A12)), and hence from (A6) the required associated wind patterns are

$$\underline{\underline{W}} = \underline{\underline{\tau}}^{obs} \, \underline{\underline{P}} \, \underline{\underline{\Lambda}}^{-1} \qquad (A16)$$

i.e.

$$\underline{w}_l = \underline{\underline{\tau}}^{obs} \, \underline{pc}_l \, \lambda_l^{-1}$$

(Effectively, the observed wind stress anomalies are projected onto the timeseries of coefficients of each of the selected SST EOFs to obtain the corresponding associated wind patterns.)

Thus the estimated wind stress anomaly pattern is

$$\underline{\tau} = \underline{\underline{W}} \, \underline{\underline{E}}^T \, \underline{T} \qquad (A17)$$

i.e. in scalar form,

$$\tau_i = \sum_{l=1}^{L} W_{il} \sum_{m=1}^{M} E_{ml} \, T_m$$

Note that the method outlined here gives a convenient one-to-one correspondence between the SST EOFs and the associated wind patterns. From (A17),

$$\underline{T} = \underline{eof}_k \quad \text{gives} \quad \underline{\tau} = \underline{w}_k \qquad (A18)$$

Note: unlike the EOFs, the associated wind patterns are not in general orthogonal.

Appendix B Principal Oscillation Pattern analysis

Principal Oscillation Pattern (POP) analysis is a general technique used to fit a first-order process to a set of data, and thus to interpret the temporal evolution of the data in terms of oscillating and decaying modes. We consider here the particular case where the data are timeseries of coefficients of empirical orthogonal functions. The basic method is outlined in section B1, spatial patterns are defined in section B2, and an option to make the oscillating patterns orthogonal is given in section B3.

B1. Basic POP analysis

Suppose that we have information about M spatial components of a system at N timepoints at intervals Δt, and that Singular Value Decomposition is applied to represent that information in terms of empirical orthogonal functions (EOFs). A subset containing L of those functions (chosen such that most of the variance of the original system is retained) is used to partially reconstruct the system as

$$\underline{\underline{Z}} = \underline{\underline{E}}\,\underline{\underline{\Lambda}}\,\underline{\underline{P}}^T \qquad (B1)$$

i.e.

$$Z_{mn} = \sum_{l=1}^{L} E_{ml}\,\lambda_l\,P_{nl}$$

(cf appendix A). Suppose that at timepoint n the spatial state of this system is denoted

$$\underline{Z}_n = \underline{\underline{E}}\,\underline{S}_n \qquad (B2)$$

where

$$\underline{S}_n = \underline{\underline{E}}^T\,\underline{Z}_n \qquad (B3)$$

Then the temporal information is contained in the $L \times N$ matrix

$$\underline{\underline{S}} = [\underline{S}_1 \;\; \cdots \;\; \underline{S}_N] = \underline{\underline{\Lambda}}\,\underline{\underline{P}}^T \qquad (B4)$$

We want to represent the evolution of the system as a first-order process that is forced by noise:

$$\underline{S}_{n+1} = \underline{\underline{\alpha}}\,\underline{S}_n + noise \qquad (B5)$$

where $\underline{\underline{\alpha}}$ is a time-independent $L \times L$ matrix, to be determined. With this form, the values $\underline{S}_n$ effectively act as predictors for $\underline{S}_{n+1}$. Write the matrix of predictors for timepoints 1 to $N-1$ as (cf appendix A, section 1)

$$\underline{\underline{A}} = [\underline{S}_1 \;\; \cdots \;\; \underline{S}_{N-1}]$$

and the 'observed' predictands as

$$\underline{\underline{F}} = [\underline{S}_2 \;\; \cdots \;\; \underline{S}_N]$$

The estimated predictands are

$$\underline{\underline{F}}^{est} = \underline{\underline{\alpha}}\ \underline{\underline{A}}$$

By minimising

$$\sum_{l=1}^{L}\sum_{n=2}^{N}(F_{ln} - F_{ln}^{est})^2$$

we find

$$\underline{\underline{\alpha}} = (\underline{\underline{F}}\,\underline{\underline{A}}^T)\,(\underline{\underline{A}}\,\underline{\underline{A}}^T)^{-1} \qquad (B6)$$

(Note that $\underline{\underline{A}}\,\underline{\underline{A}}^T$ corresponds to a lag-0 covariance matrix and $\underline{\underline{F}}\,\underline{\underline{A}}^T$ to a lag-1 covariance matrix.)

We next determine the normal modes of the system, by finding L eigenvalues η and eigenvectors $\underline{e}$ of $\underline{\underline{\alpha}}$:

$$\underline{\underline{\alpha}}\ \underline{e} = \eta\,\underline{e} \qquad (B7)$$

The ηs and $\underline{e}$s are complex in general, but, because $\underline{\underline{\alpha}}$ is real, the complex values occur in complex conjugate pairs and real η implies real $\underline{e}$.

For real η, the evolution of the free mode is simple growth or decay, with e-folding time $-\Delta t/\ln|\eta|$. For complex η, consider real and imaginary parts

$$\eta = \eta_R + i\,\eta_I \quad , \quad \underline{e} = \underline{e}_R + i\,\underline{e}_I$$

Put

$$\eta = \rho\,e^{i\omega}$$

where

$$\rho = (\eta_R^2 + \eta_I^2)^{1/2} \quad , \quad \omega = \arctan(\eta_I/\eta_R)$$

Then (B7) gives

$$\underline{\underline{\alpha}}\ [\underline{e}_R\ \ \underline{e}_I] = \rho\ [\underline{e}_R\ \ \underline{e}_I] \begin{bmatrix} \cos\omega & \sin\omega \\ -\sin\omega & \cos\omega \end{bmatrix} \qquad (B8)$$

Thus these complex modes represent oscillations, with period $\tau = (2\pi/|\omega|)\Delta t$ and decay time $D = -\Delta t/\ln\rho$, changing between system states represented by $\underline{e}_R$ and $\underline{e}_I$. For example, if the unforced system is represented by $\underline{e}_R$ at time t, then it changes to $-\underline{e}_I\ e^{-\tau/4D}$ at time $t+\tau/4$, then to $-\underline{e}_R\ e^{-\tau/2D}$ at $t+\tau/2$, then to $\underline{e}_I\ e^{-3\tau/4D}$ at $t+3\tau/4$, then to $\underline{e}_R\ e^{-\tau/D}$ at $t+\tau$, etc.

Note that in continuous form the complex amplitude a of an oscillating mode evolves freely as

$$a(t) = a_0\ e^{i2\pi t/\tau}\ e^{-t/D} \qquad (B9)$$

The evolution of the system can now be interpreted in terms of these modes. Construct a basis matrix $\underline{\underline{B}}$ from the eigenvectors $\underline{e}$, by taking as its columns $\underline{e}_R$ and $\underline{e}_I$ from one of each complex conjugate pair together with the real $\underline{e}$s. Because $\underline{\underline{\alpha}}$ is real, there

are L such columns and they usually form a complete set. Suppose there are $K \leq L$ complex eigenvalue pairs. For convenience, suppose $\underline{\underline{B}}$ is ordered with the oscillating components first:

$$\underline{\underline{B}} = [\underline{e}_{R1} \quad \underline{e}_{I1} \quad \cdots \quad \underline{e}_{RK} \quad \underline{e}_{IK} \quad \cdots \quad \underline{e}_{L}] \tag{B10}$$

At any timepoint n the state of the system can be re-expressed in terms of these basis vectors $\underline{b}$:

$$\underline{S}_n = \underline{\underline{B}}\ \underline{Y}_n \tag{B11}$$

With this transformation the evolution equation (B5) becomes

$$\begin{aligned} \underline{Y}_{n+1} &= \underline{\underline{B}}^{-1}\ \underline{\underline{\alpha}}\ \underline{\underline{B}}\ \underline{Y}_n + \textit{transformed noise} \\ &= \underline{\underline{\beta}}\ \underline{Y}_n + \textit{transformed noise} \end{aligned} \tag{B12}$$

where

$$\underline{\underline{\beta}} = \underline{\underline{B}}^{-1}\ \underline{\underline{\alpha}}\ \underline{\underline{B}} = \begin{bmatrix} \rho_1 \cos\omega_1 & \rho_1 \sin\omega_1 & 0 & 0 & \cdots & 0 \\ -\rho_1 \sin\omega_1 & \rho_1 \cos\omega_1 & 0 & 0 & \cdots & 0 \\ 0 & 0 & \rho_2 \cos\omega_2 & \rho_2 \sin\omega_2 & \cdots & 0 \\ 0 & 0 & -\rho_2 \sin\omega_2 & \rho_2 \cos\omega_2 & \cdots & 0 \\ \vdots & & & & \ddots & \vdots \\ 0 & 0 & 0 & 0 & \cdots & \eta_L \end{bmatrix}$$

is the matrix controlling the oscillations and decays of the independent normal modes.

B2. Spatial patterns and their timeseries

Using (B2) and (B11) the spatial state at timepoint n can be written

$$\underline{Z}_n = \underline{\underline{E}}\ \underline{S}_n = \underline{\underline{E}}\ \underline{\underline{B}}\ \underline{Y}_n = \underline{\underline{POP}}\ \underline{Y}_n \tag{B13}$$

where

$$\begin{aligned} \underline{\underline{POP}} = \underline{\underline{E}}\ \underline{\underline{B}} &= \underline{\underline{E}}\ [\underline{e}_{R1} \quad \underline{e}_{I1} \quad \cdots \quad] \\ &= [\underline{pop}_{R1} \quad \underline{pop}_{I1} \quad \cdots \quad] \end{aligned} \tag{B14}$$

Instead of spatial EOF patterns, the system is now represented by spatial POPs which are linear combinations of the EOFs. Note that the sequence of spatial patterns found as an individual POP mode evolves is

$$\underline{pop}_R \rightarrow -\underline{pop}_I \rightarrow -\underline{pop}_R \rightarrow \underline{pop}_I \rightarrow \underline{pop}_R \rightarrow \tag{B15}$$

The system $\underline{\underline{Z}}$ can be regarded as superimposed oscillating and decaying POPs that are forced by noise: from (B12) and (B13),

$$\underline{Z}_{n+1} = \underline{\underline{POP}} \, (\, \underline{\underline{\beta}} \, \underline{Y}_n + \textit{transformed noise} \,) \qquad (B16)$$

Denote the timeseries of coefficients of POPs by $\underline{popt}$ and define the $L \times N$ matrix

$$\underline{\underline{POPT}} = [\underline{popt}_{R1} \quad \underline{popt}_{I1} \quad \ldots \quad]$$

Then (B1) can be written in the form

$$\underline{\underline{Z}} = \underline{\underline{POP}} \, \underline{\underline{POPT}}^T \qquad (B17)$$

where

$$\underline{\underline{POPT}}^T = [\underline{Y}_1 \quad \underline{Y}_2 \quad \ldots \quad]$$

Note that from (B11) and (B4)

$$\begin{aligned} \underline{\underline{POPT}} &= \underline{\underline{S}}^T \, (\underline{\underline{B}}^{-1})^T \\ &= \underline{\underline{P}} \, \underline{\underline{\Lambda}} \, (\underline{\underline{B}}^{-1})^T \end{aligned} \qquad (B18)$$

Thus the POP timeseries in this case are transformed principal components.

B3 Orthogonal oscillating patterns

The eigenvalues in (B7) are defined to within an arbitrary complex multiple. We can choose this multiple such that

$$|\underline{e}| = 1 \qquad (B19a)$$

and, if complex,

$$\underline{e}_R^T \, \underline{e}_I = 0 \qquad (B19b)$$

($\underline{e}$ is then uniquely defined.) A useful consequence of this choice is that the POP spatial patterns corresponding to $\underline{e}_R$ and $\underline{e}_I$ for an oscillating mode are orthogonal. Using $\underline{\underline{E}}^T \, \underline{\underline{E}} = \underline{\underline{I}}$,

$$\begin{aligned} \underline{pop}_R^T \, \underline{pop}_I &= \underline{e}_R^T \, \underline{\underline{E}}^T \, \underline{\underline{E}} \, \underline{e}_I \\ &= \underline{e}_R^T \, \underline{e}_I \\ &= 0 \end{aligned} \qquad (B20a)$$

Further,

$$\underline{pop}_R^T \, \underline{pop}_R + \underline{pop}_I^T \, \underline{pop}_I = 1 \qquad (B20b)$$

Note, however, that spatial patterns from separate POP modes are not generally orthogonal.

B4 Variance

Suppose $\underline{\underline{Z}}$ is partially reconstructed using the kth oscillating POP mode:

$$\underline{\underline{Z}}_k^{part} = [\underline{pop}_{Rk} \quad \underline{pop}_{Ik}] \begin{bmatrix} \underline{popt}_{Rk}^T \\ \underline{popt}_{Ik}^T \end{bmatrix}$$

Using (B20) we find that the partial variance V_k is

$$V_k = Var(\underline{\underline{Z}}_k^{part}) = \underline{popt}_{Rk}^2 + \underline{popt}_{Ik}^2 \qquad (B21)$$

Note that, in contrast to SVD, the partial variances cannot simply be added to obtain $Var(\underline{\underline{Z}})$.

Table 1: Starting times of prediction experiments for case studies. The 20 experiments marked (*) are included in Fig.5a and used for the correlations in Fig.5b.

case:	72/73, warm	73/74, cold	82/83, warm	86/87, warm	87/88, cold	74/75
	Jul/71	Jul/72	Jul/81	Jan/86	Apr/87	
	Oct/71*	Oct/72*	Oct/81*	Apr/86*	Jul/87*	Jan/74
	Jan/72*	Jan/73*	Jan/82*	Jul/86*	Oct/87*	Apr/74
	Apr/72*	Apr/73*	Apr/82*	Oct/86*	Jan/88*	Jul/74
	Jul/72*	Jul/73*	Jul/82*	Jan/87*	Apr/88*	Oct/74

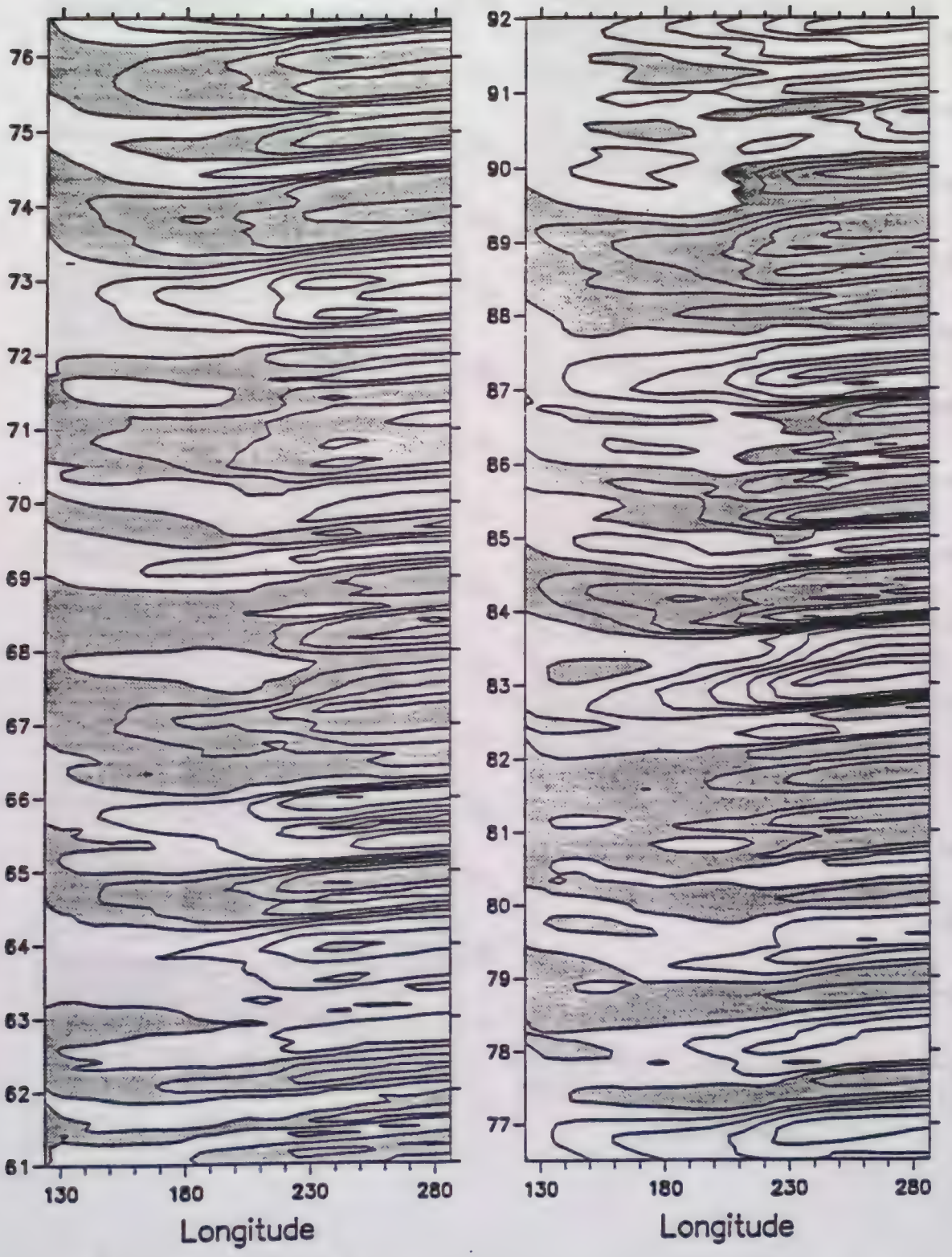

Fig. 1a: Model sea surface temperature anomalies along the equator, from the simulation forced by detrended FSU wind stress anomalies. Contour interval 0.5°C, negative values shaded.

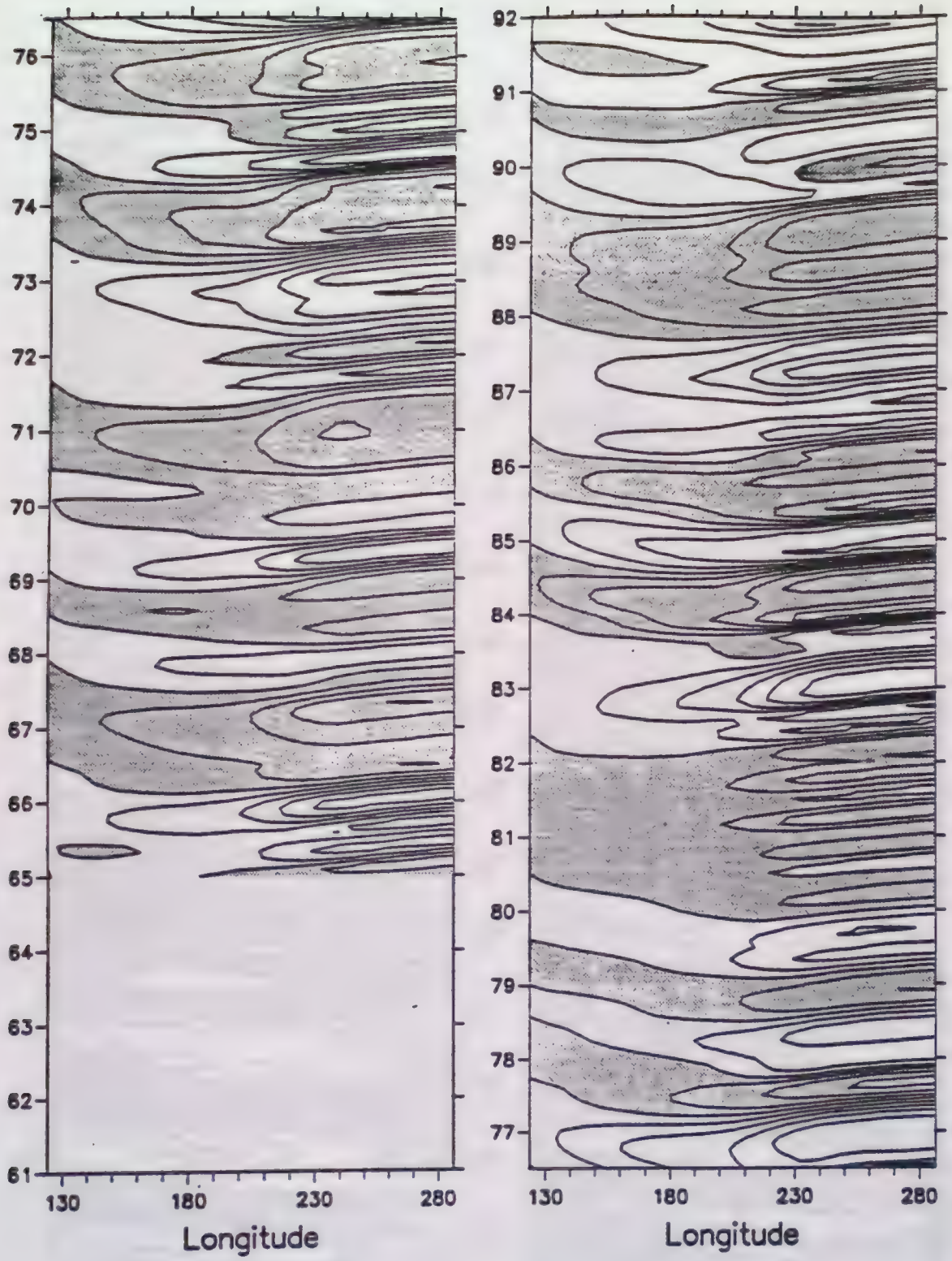

Fig. 1b: Model sea surface temperature anomalies along the equator, from the simulation forced by wind stress anomalies reconstructed using 3 SST EOFs. Contour interval 0.5°C, negative values shaded.

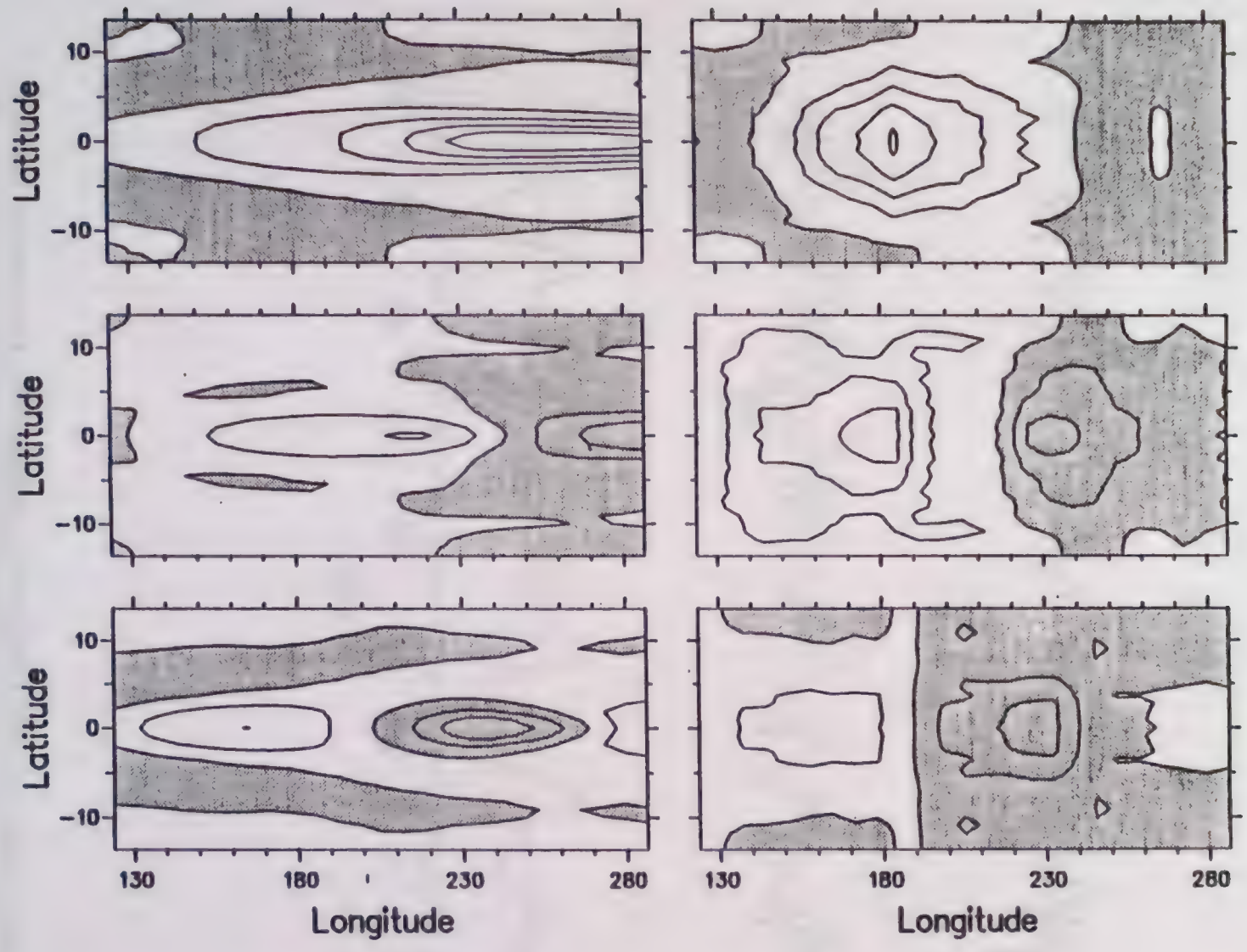

Fig. 2a: The first (top), second (middle), and third (bottom) EOF patterns of simulated SST anomalies (left), and associated zonal wind stress anomalies (right). Contour intervals are arbitrary, negative values are shaded.

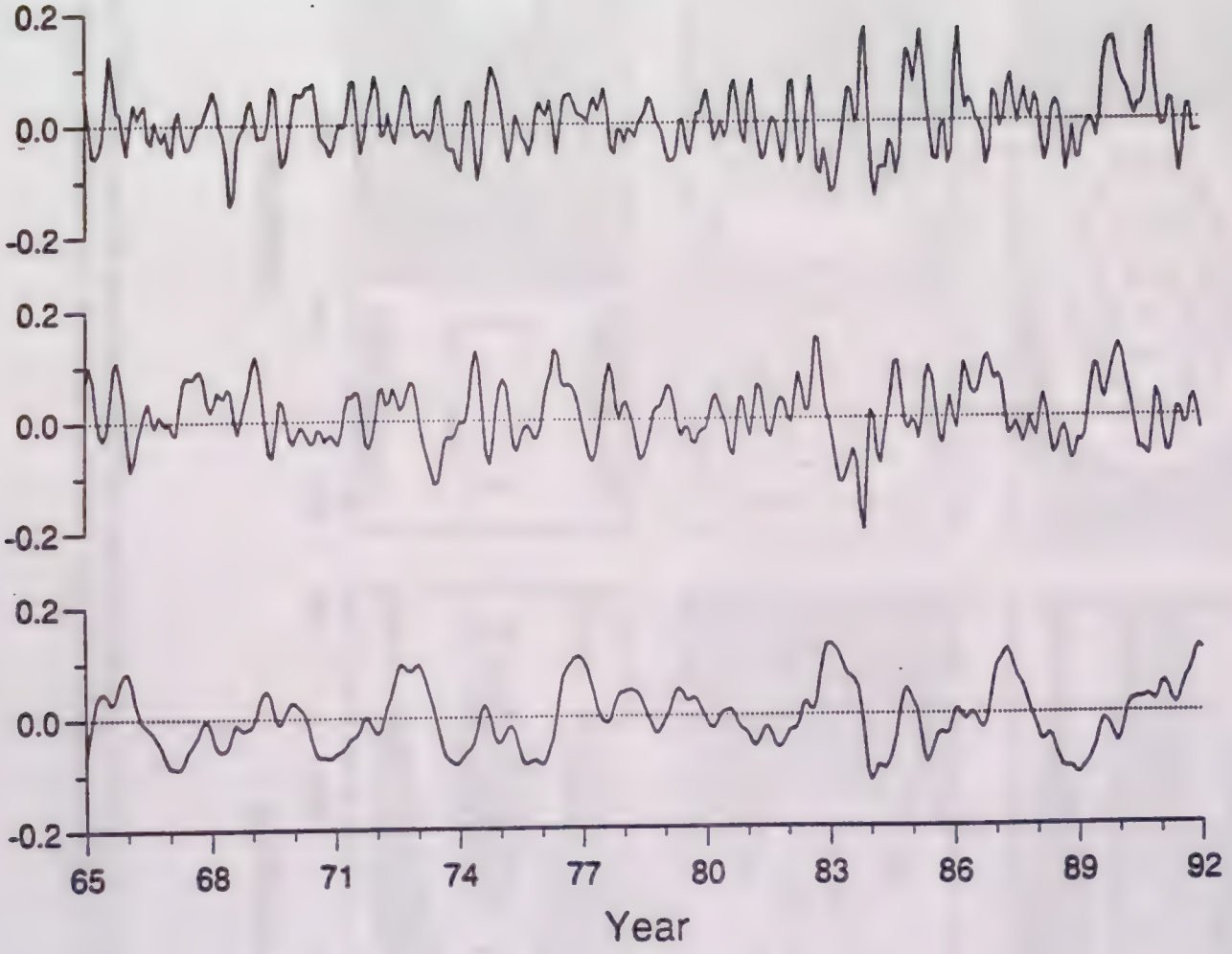

Fig. 2b: Principal component timeseries corresponding to the first (bottom), second (middle) and third (top) EOFs of model simulated SST anomalies, calculated for the period 1965-1992.

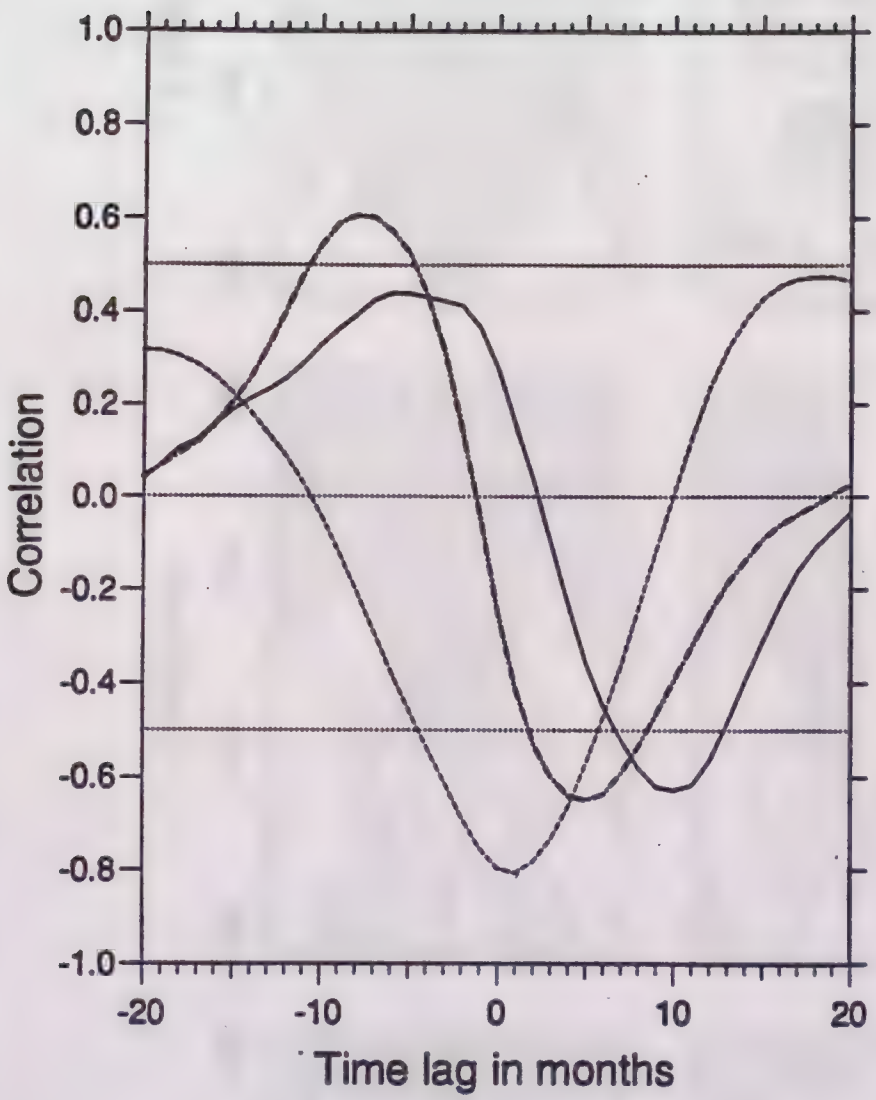

Fig. 3a: Lag correlations calculated using timeseries of observed Nino3 SST anomalies, and coefficients of real and imaginary Principal Oscillation Patterns for the dominant ENSO mode in the simulation run. Solid line is correlation of real POP and Nino3, dashed is imaginary POP and Nino3, dash-dot is imaginary POP and real POP. Negative lags imply that real POP leads (solid), imaginary POP leads (dashed, dash-dot).

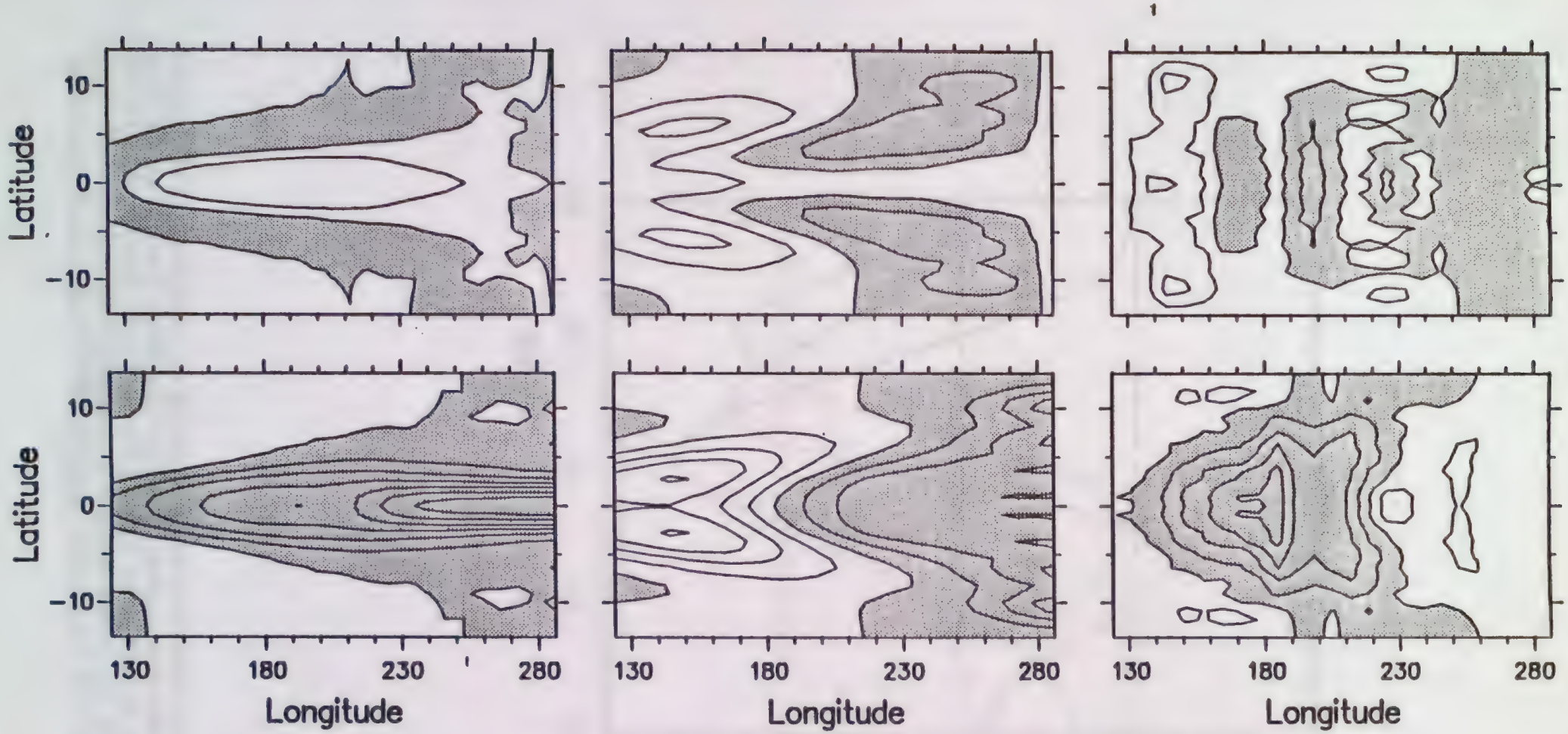

Fig. 3b: Spatial patterns of anomalies of SST (left), layer depth (middle), zonal wind stress (right) for the dominant ENSO-related POP mode in the simulation run. The POP mode has period 31.5 months and e-folding decay time 17 months. Real (top) patterns are associated with transition ENSO phase, while imaginary (bottom) patterns are associated with peak ENSO phase. Contour intervals are arbitrary for each physical field, but are the same for the real and imaginary components. Negative values are shaded.

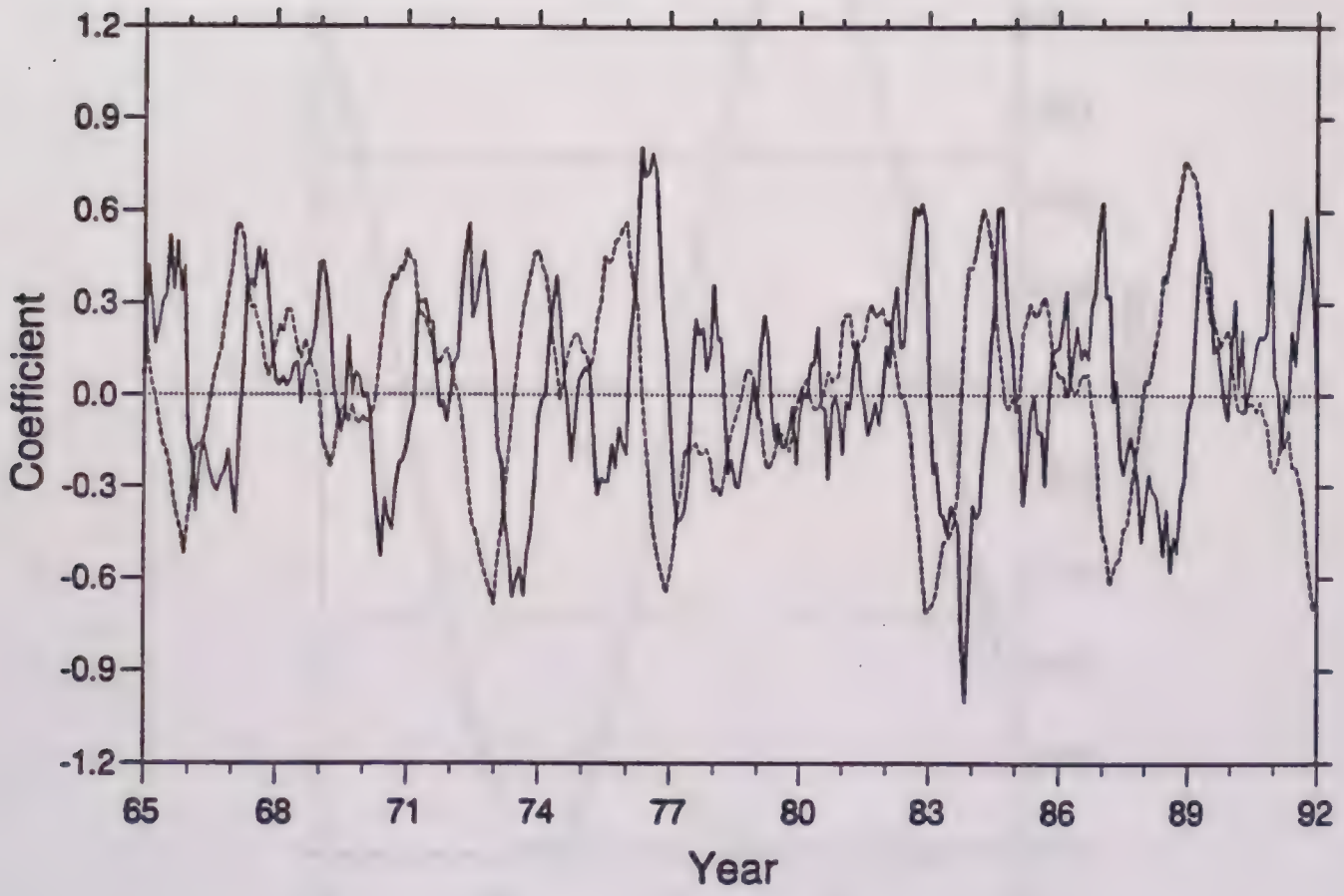

Fig. 3c: Timeseries of coefficients of the real (solid) and imaginary (dashed) POP patterns shown in Fig. 3b for the simulation run. For plotting purposes, the coefficients are scaled such that the maximum absolute value is 1.

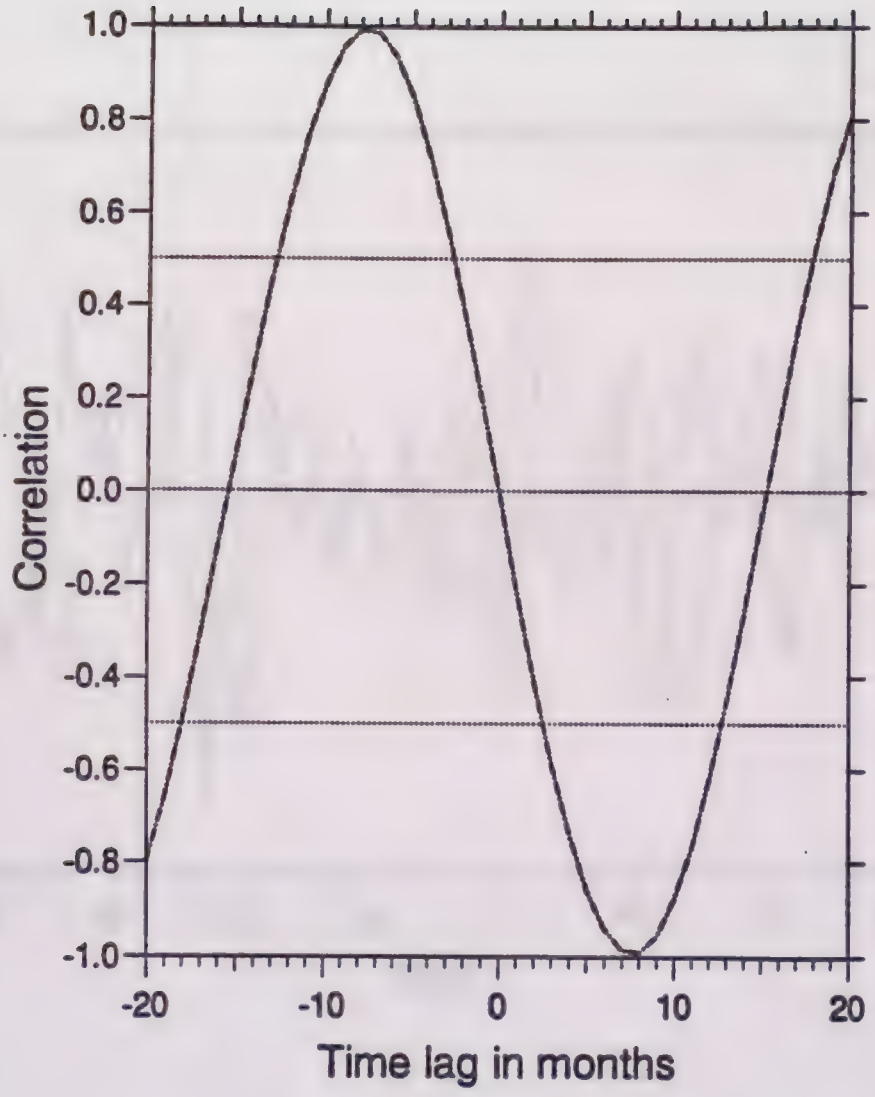

Fig. 4a: Lag correlation calculated using timeseries of coefficients of real and imaginary Principal Oscillation Patterns for the dominant ENSO mode in the free coupled run. Negative lag implies that imaginary POP leads the real POP.

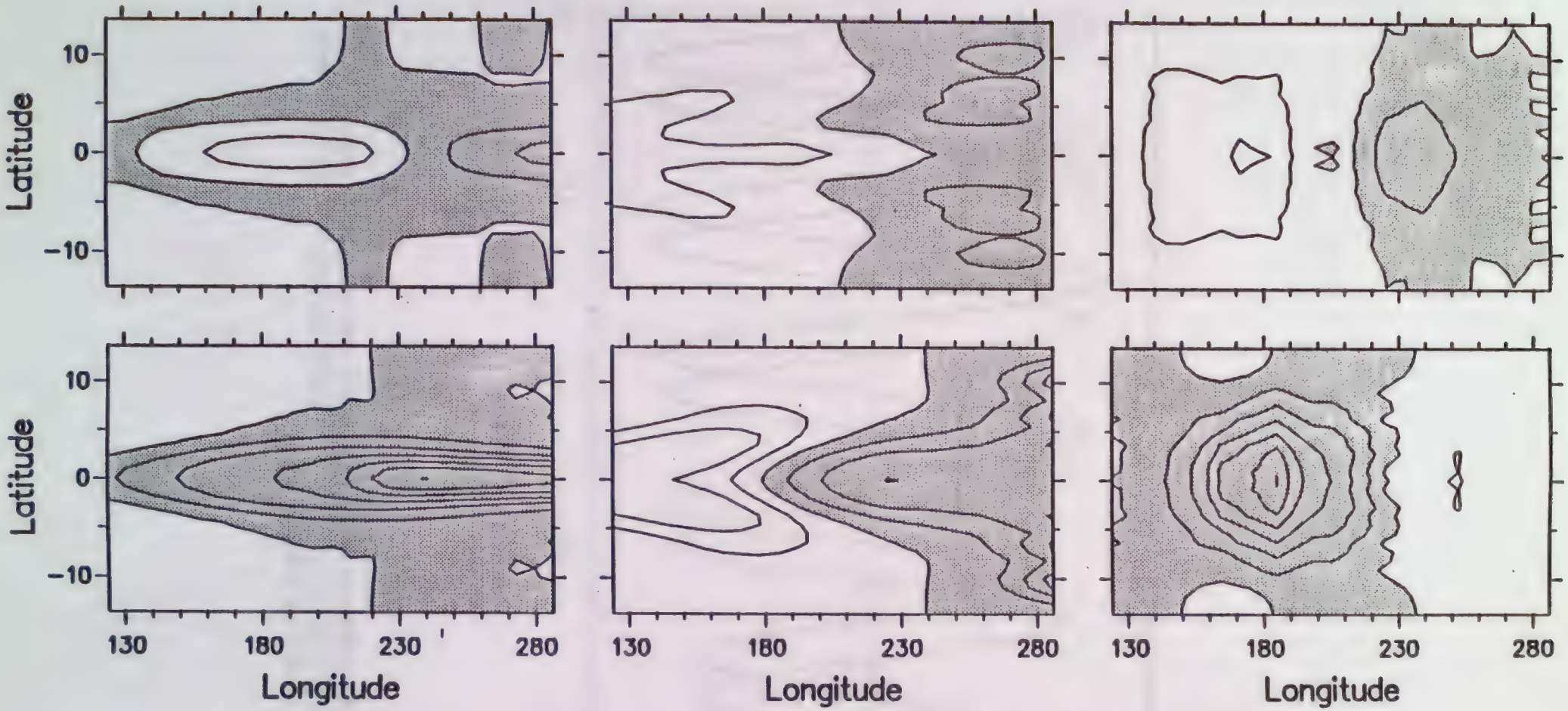

Fig. 4b: Spatial patterns of anomalies of SST (left), layer depth (middle), zonal wind stress (right) for the dominant ENSO-related POP mode in the free coupled run. The POP mode has period 30.6 months. Real (top) patterns are associated with transition ENSO phase, while imaginary (bottom) patterns are associated with peak ENSO phase. Contour intervals are arbitrary for each physical field, but are the same for the real and imaginary components. Negative values are shaded.

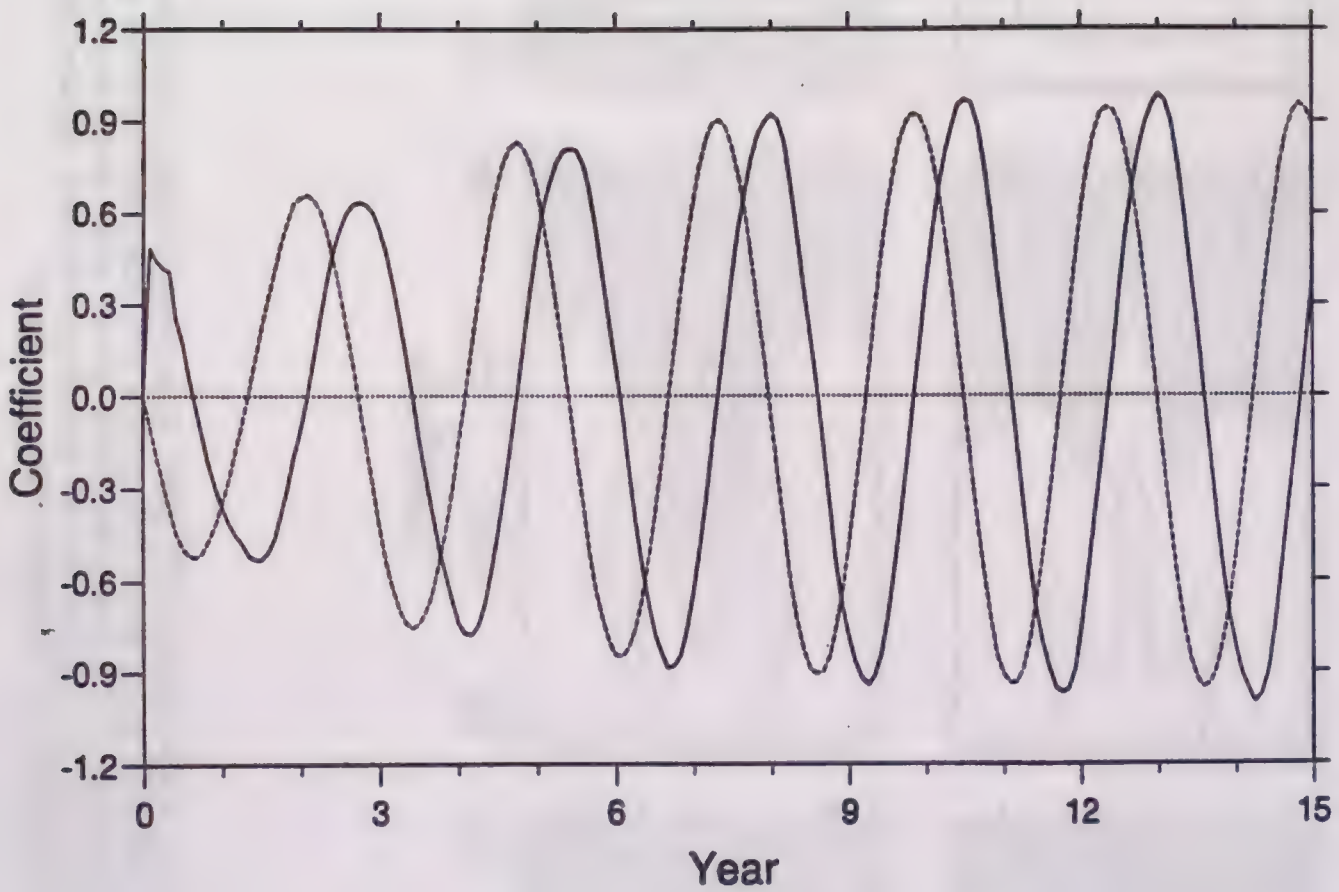

Fig. 4c: Timeseries of coefficients of the real (solid) and imaginary (dashed) POP patterns shown in Fig. 4b for the free coupled run. For plotting purposes, the coefficients are scaled such that the maximum absolute value is 1.

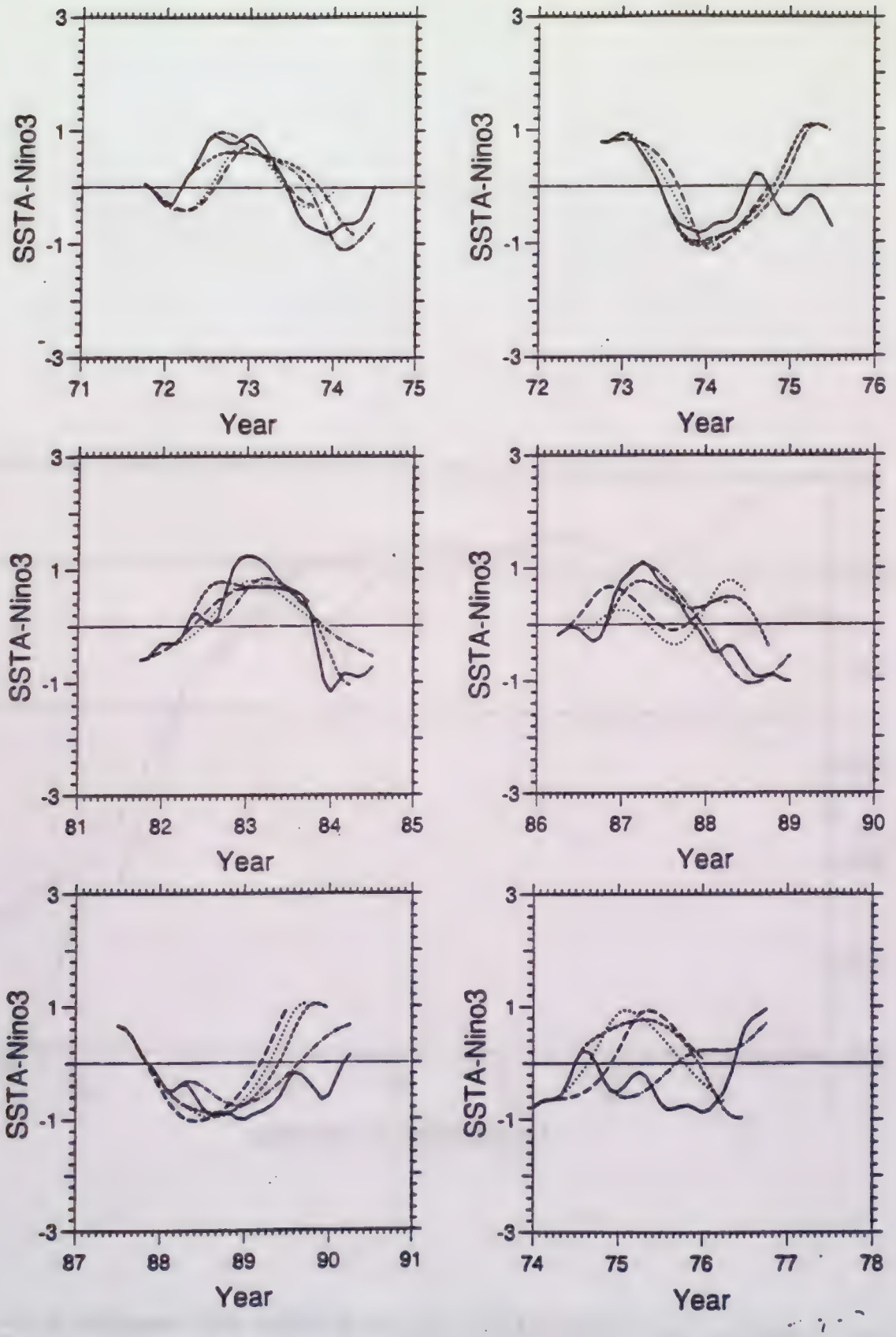

Fig. 5a: SST anomalies in the Nino3 region for the simulation run (solid) and predictions using the empirical atmosphere (dashed), for 5 warm and cold ENSO cases and for the 74/75 non-event (see Table 1). Units are °C. Initial conditions for the predictions were taken from the simulation run.

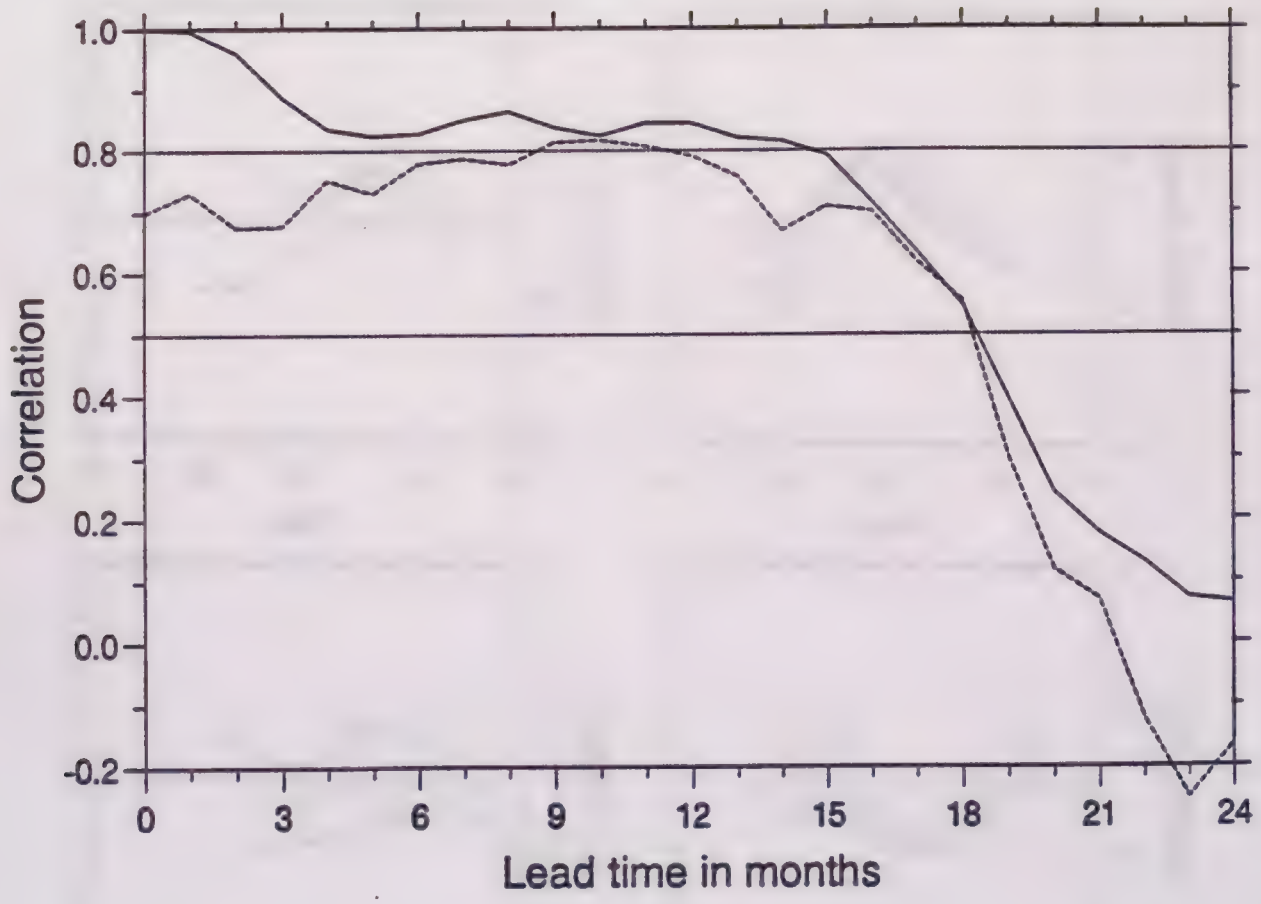

Fig. 5b: Correlation, as a function of lead time, of predicted SST anomalies in the Nino3 region with simulated (solid) and observed (dashed) values. 20 predictions for 5 warm and cold ENSO cases were used (see Table 1).

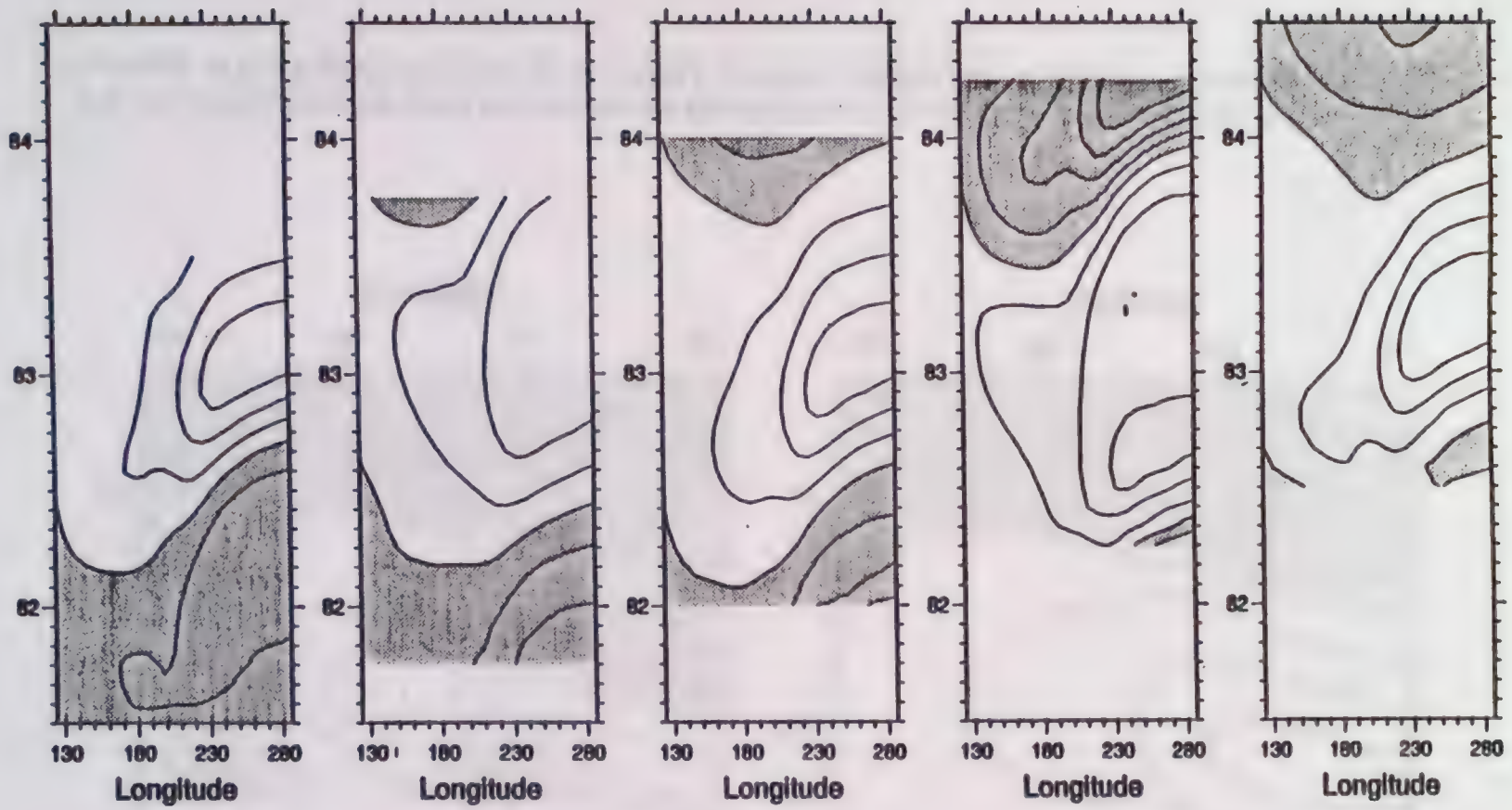

Fig. 6a: SST anomalies along the equator for 5 individual predictions of the 82/83 warm event. Contour interval 0.5°C, negative values shaded.

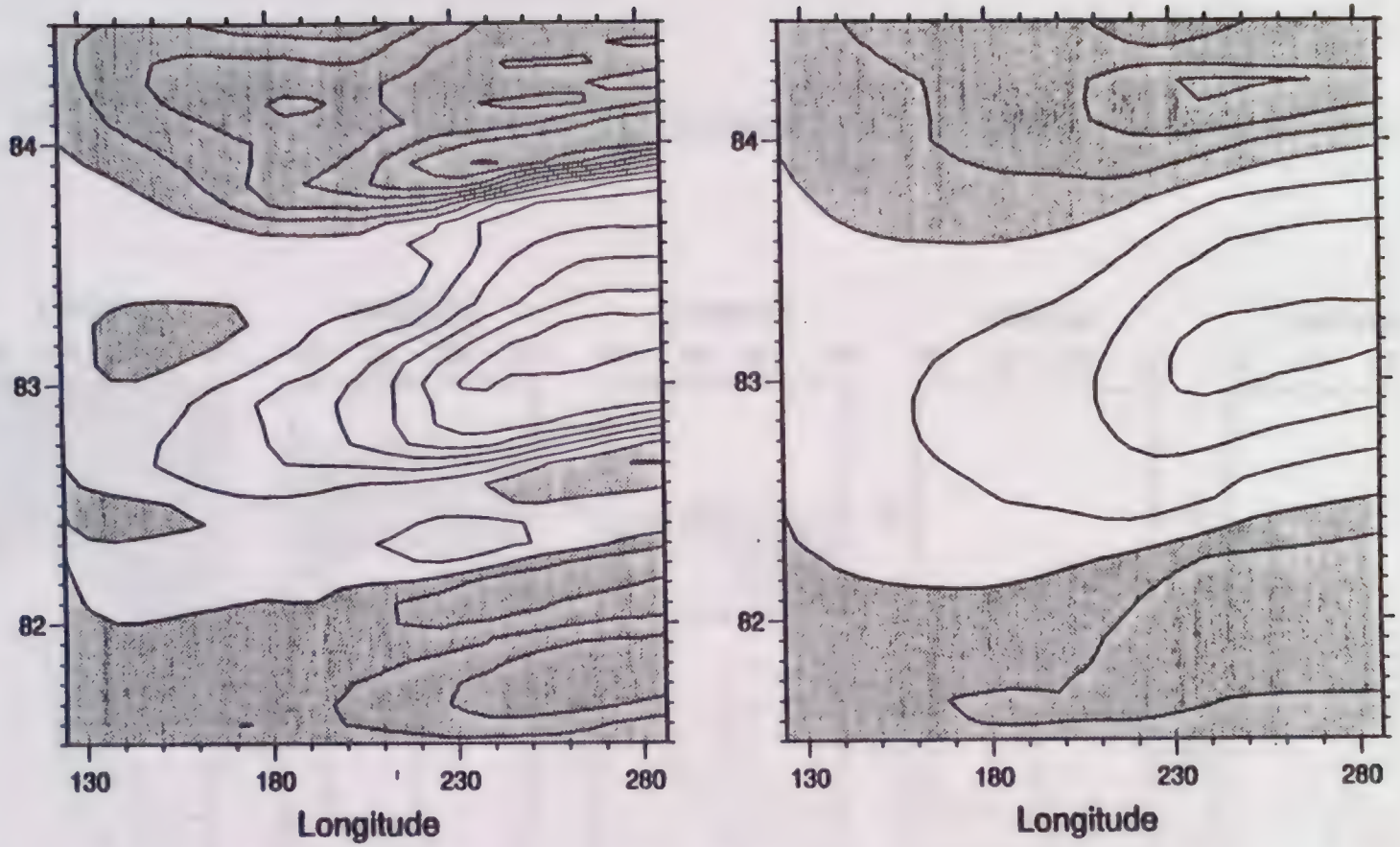

Fig. 6b: SST anomalies along the equator for the 82/83 warm event from the simulation (left) and from the average of the 5 predictions in Fig. 6a (right). Contour interval 0.5°C, negative values shaded.

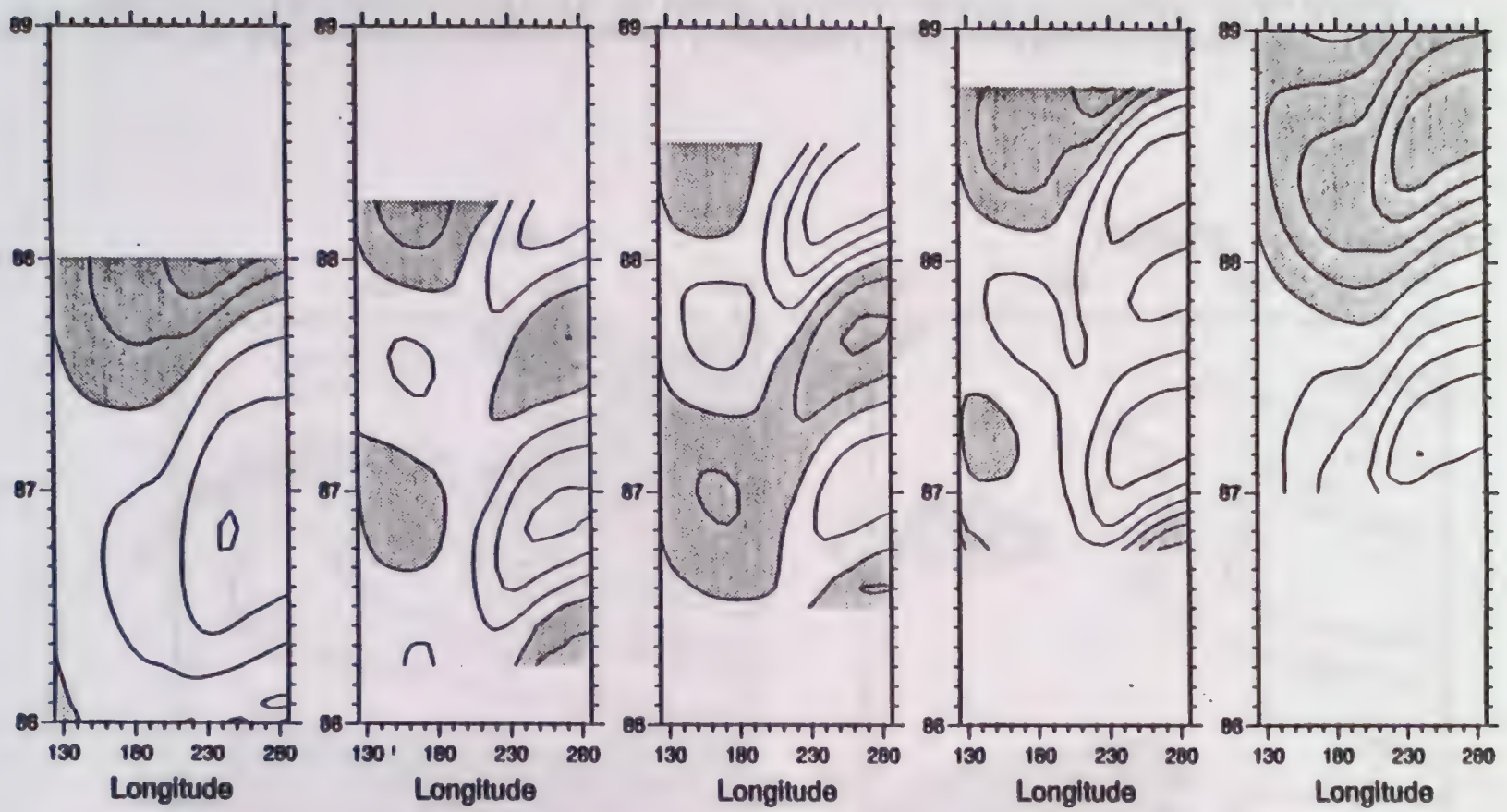

Fig. 7a: SST anomalies along the equator for 5 individual predictions of the 86/87 warm event. Contour interval 0.5°C, negative values shaded.

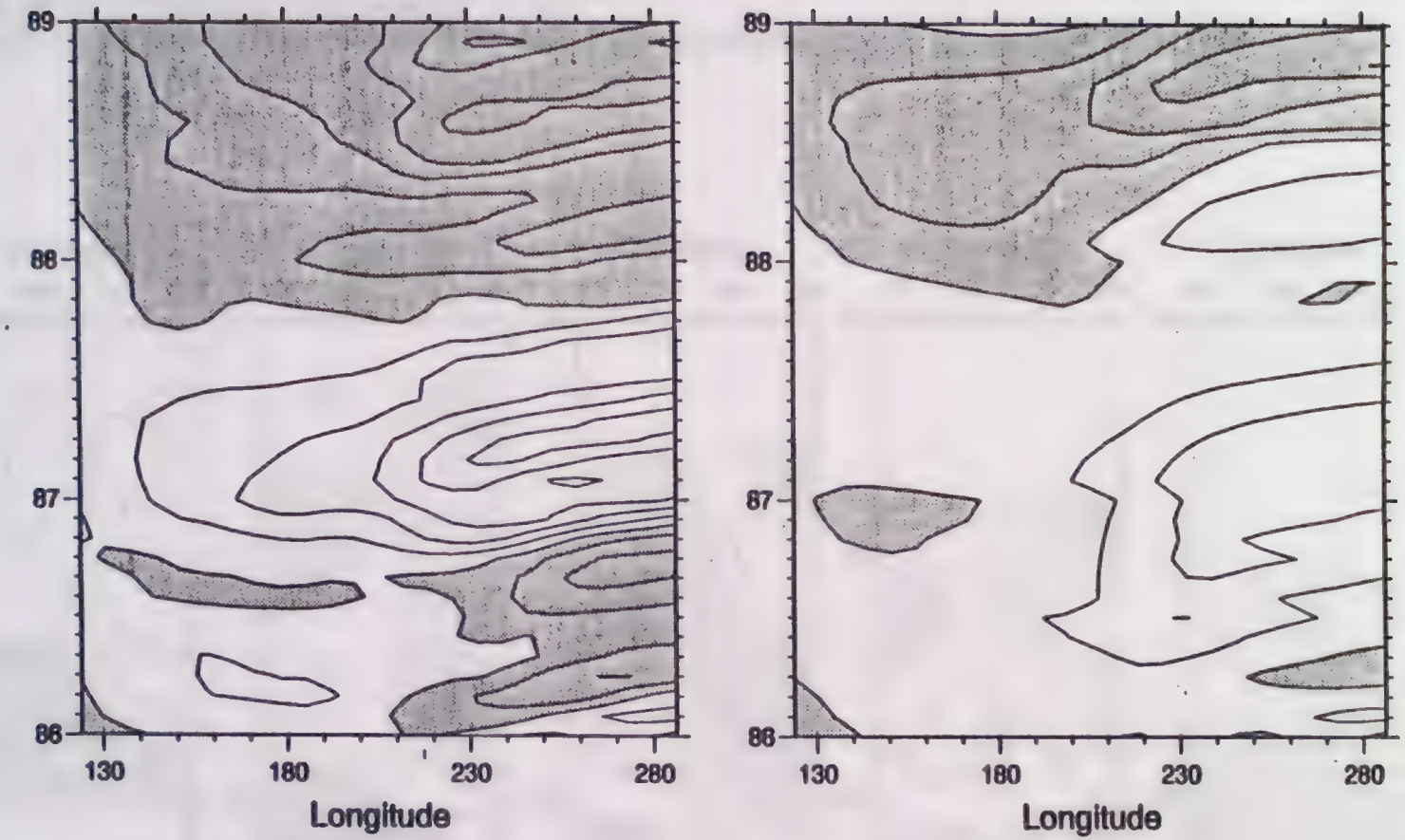

Fig. 7b: SST anomalies along the equator for the 86/87 warm event from the simulation (left) and from the average of the 5 predictions in Fig. 7a (right). Contour interval 0.5°C, negative values shaded.

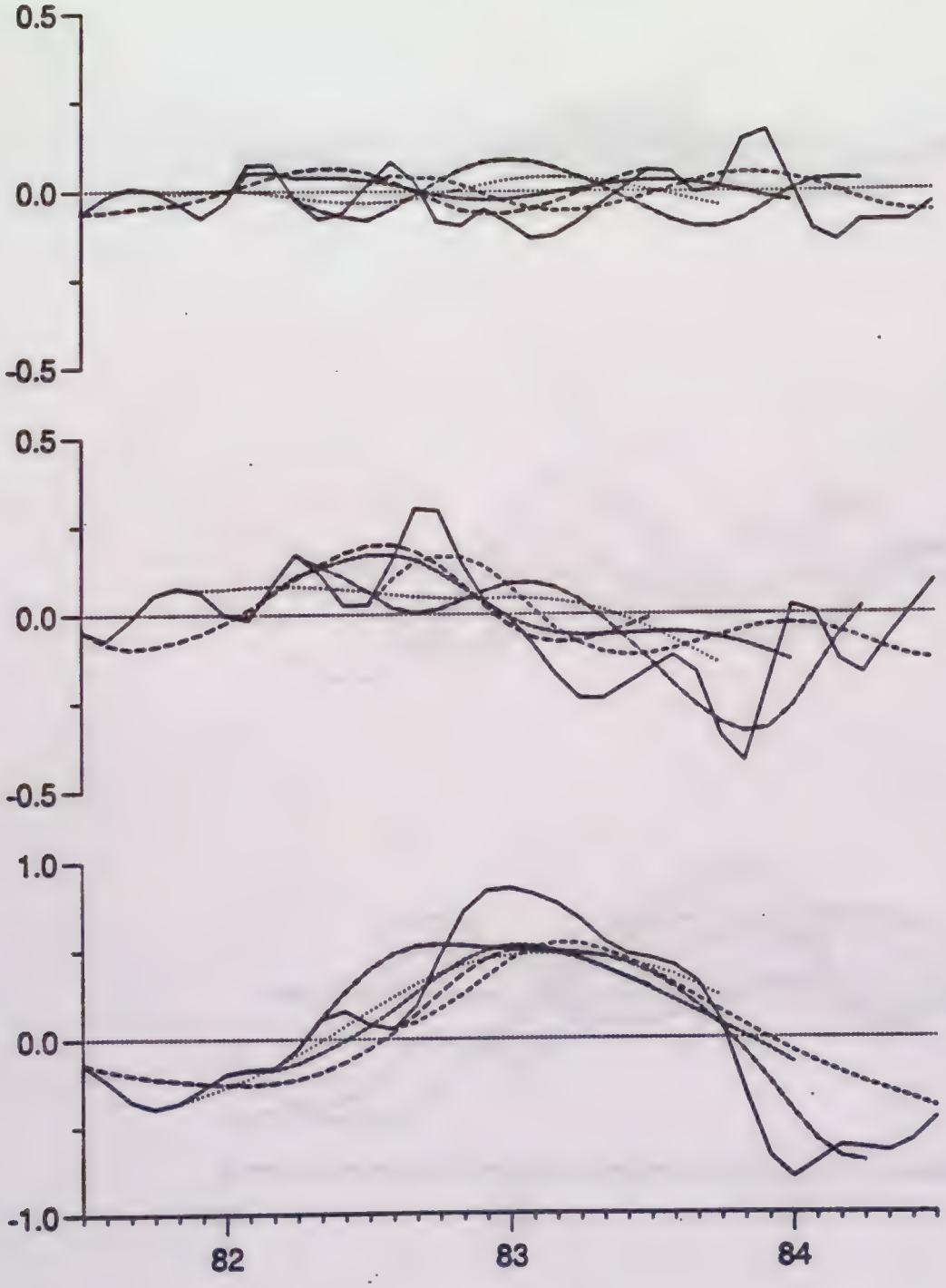

Fig. 8a: Timeseries of coefficients A_k for the first (bottom), second (middle) and third (top) EOFs of SST anomalies for the 82/83 warm event, for the control run (solid) and 5 predictions (broken lines). Note the different scales for the first and higher EOFs.

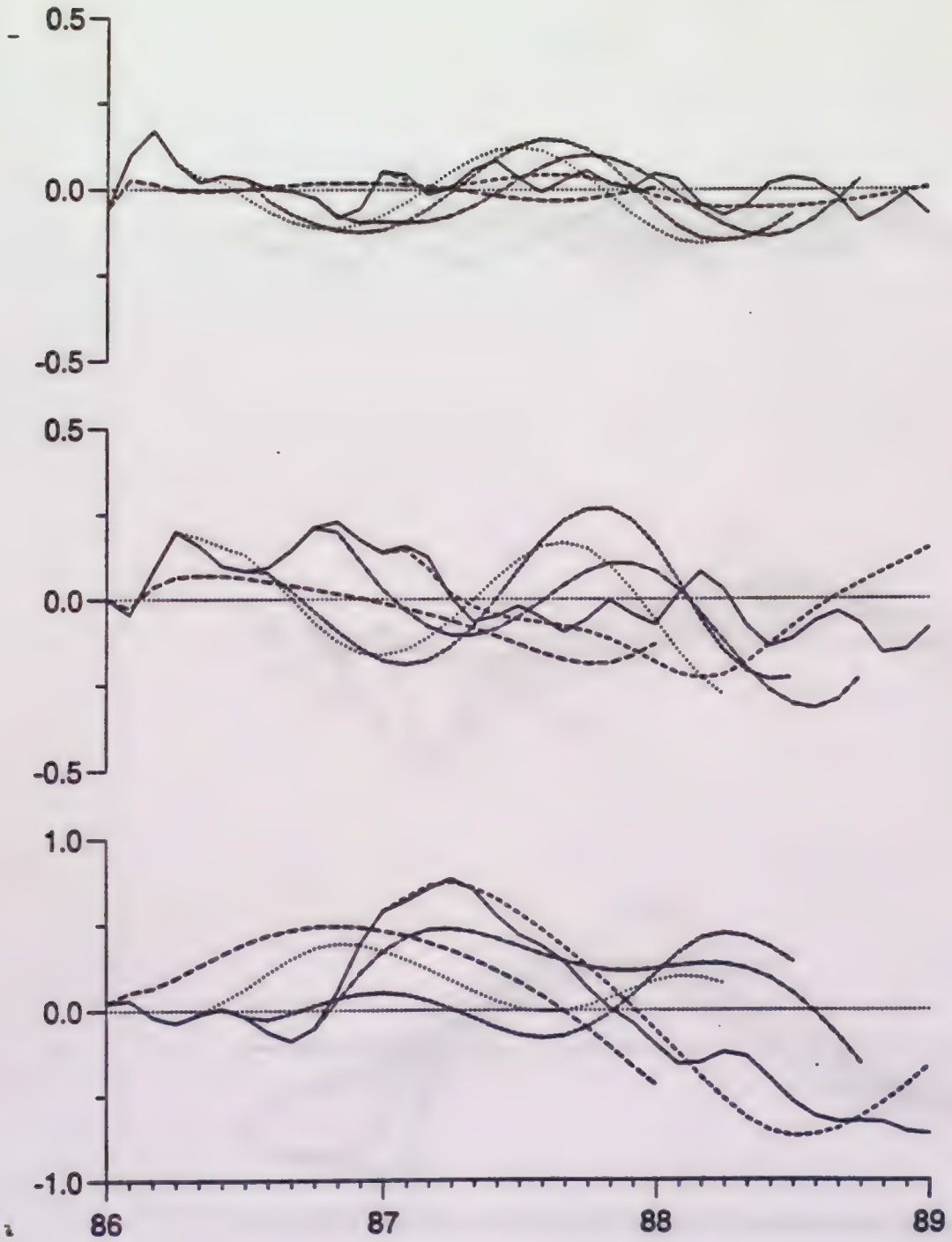

Fig. 8b: Timeseries of coefficients A_k for the first (bottom), second (middle) and third (top) EOFs of SST anomalies for the 86/87 warm event, for the control run (solid) and 5 predictions (broken lines). Note the different scales for the first and higher EOFs.

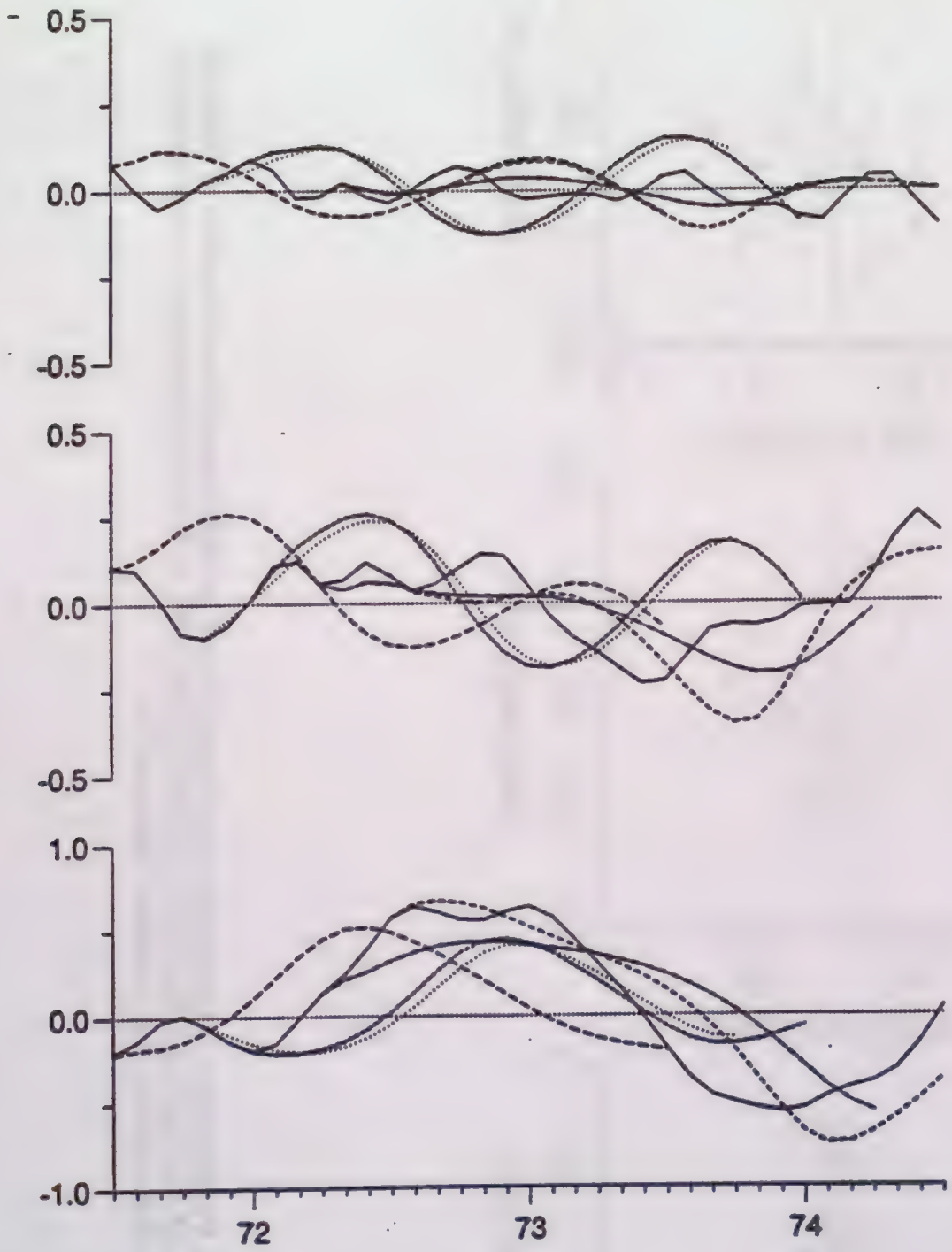

Fig. 8c: Timeseries of coefficients A_k for the first (bottom), second (middle) and third (top) EOFs of SST anomalies for the 72/73 warm event, for the control run (solid) and 5 predictions (broken lines). Note the different scales for the first and higher EOFs.

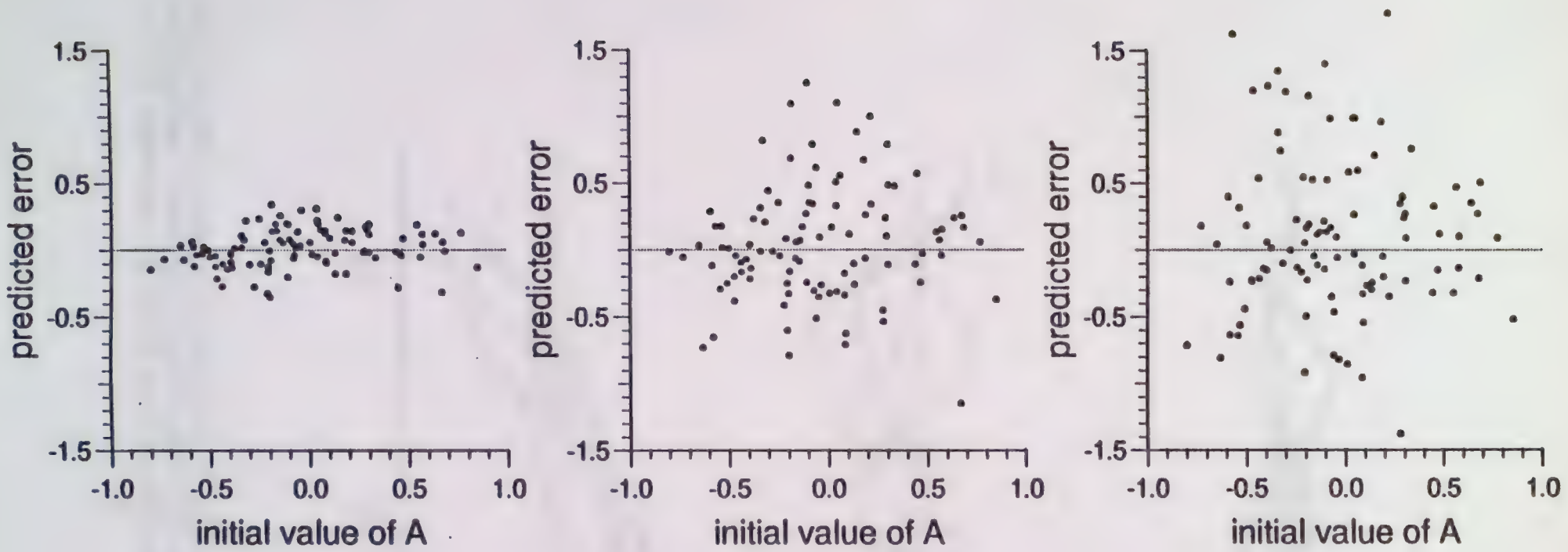

Fig. 9a: Prediction errors (prediction minus control) for Niño3 SST anomalies as a function of the initial value A_{1t_0} of the coefficient associated with EOF1, from 100 prediction experiments, for lead times of 3 (left), 6 (middle) and 9 (right) months. Units are °C.

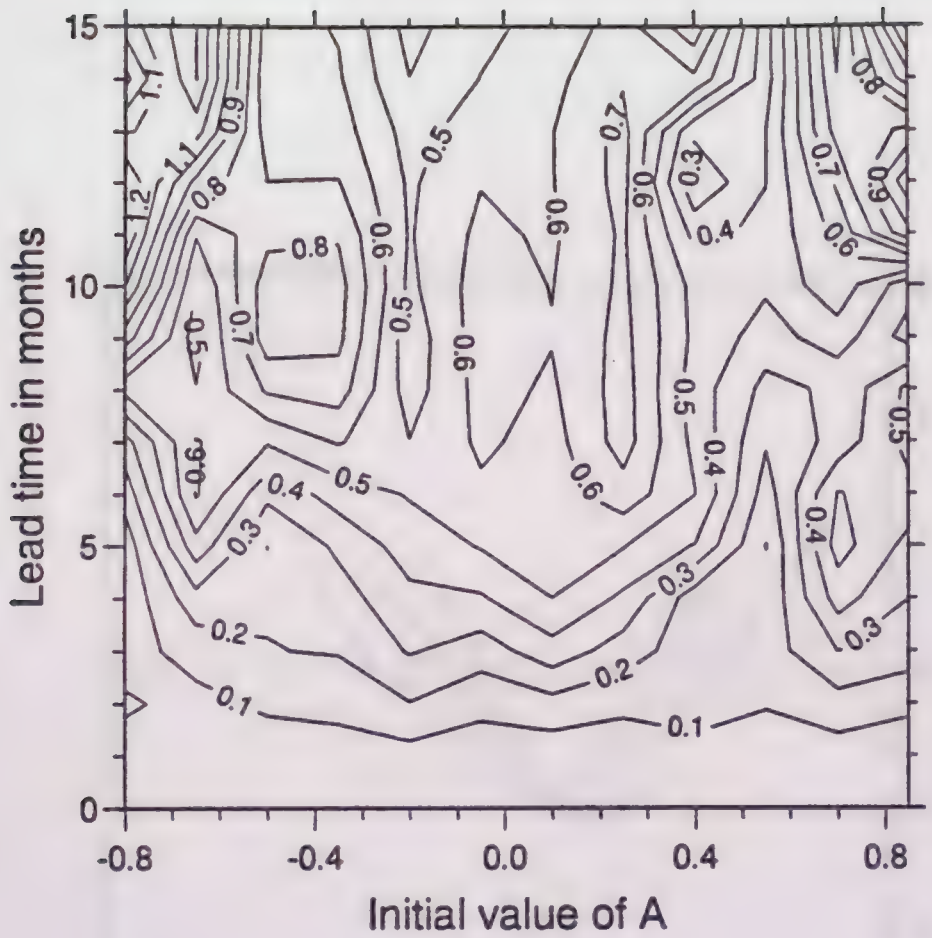

Fig. 9b: RMS values of prediction errors (prediction - control) as a function of lead time and of the initial value A_{1t_0} of the coefficient associated with EOF1. Errors from 100 prediction experiments are grouped into bins with values of A_{1t_0} centred on -0.8+0.15i, i=0...11. Units are °C.

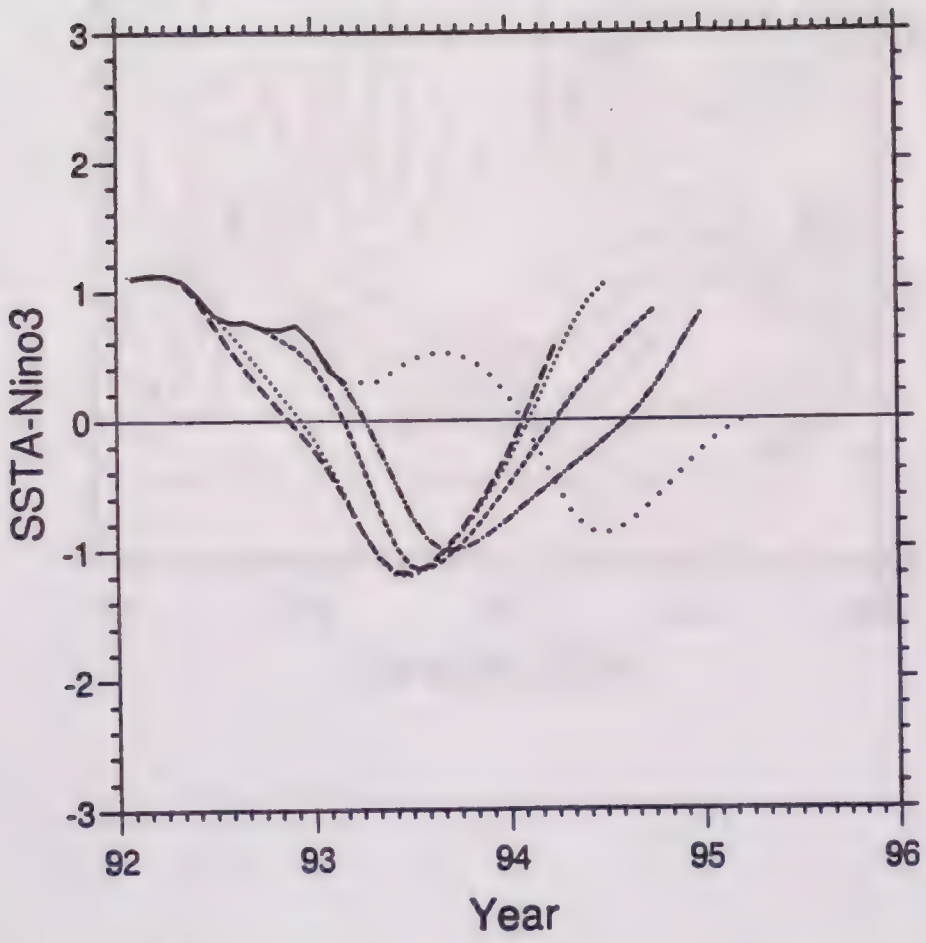

Fig. 10: SST anomalies for the Niño3 region for forecast experiments starting April 1992, July 1992, October 1992, January 1993, and March 1993. Units are °C.

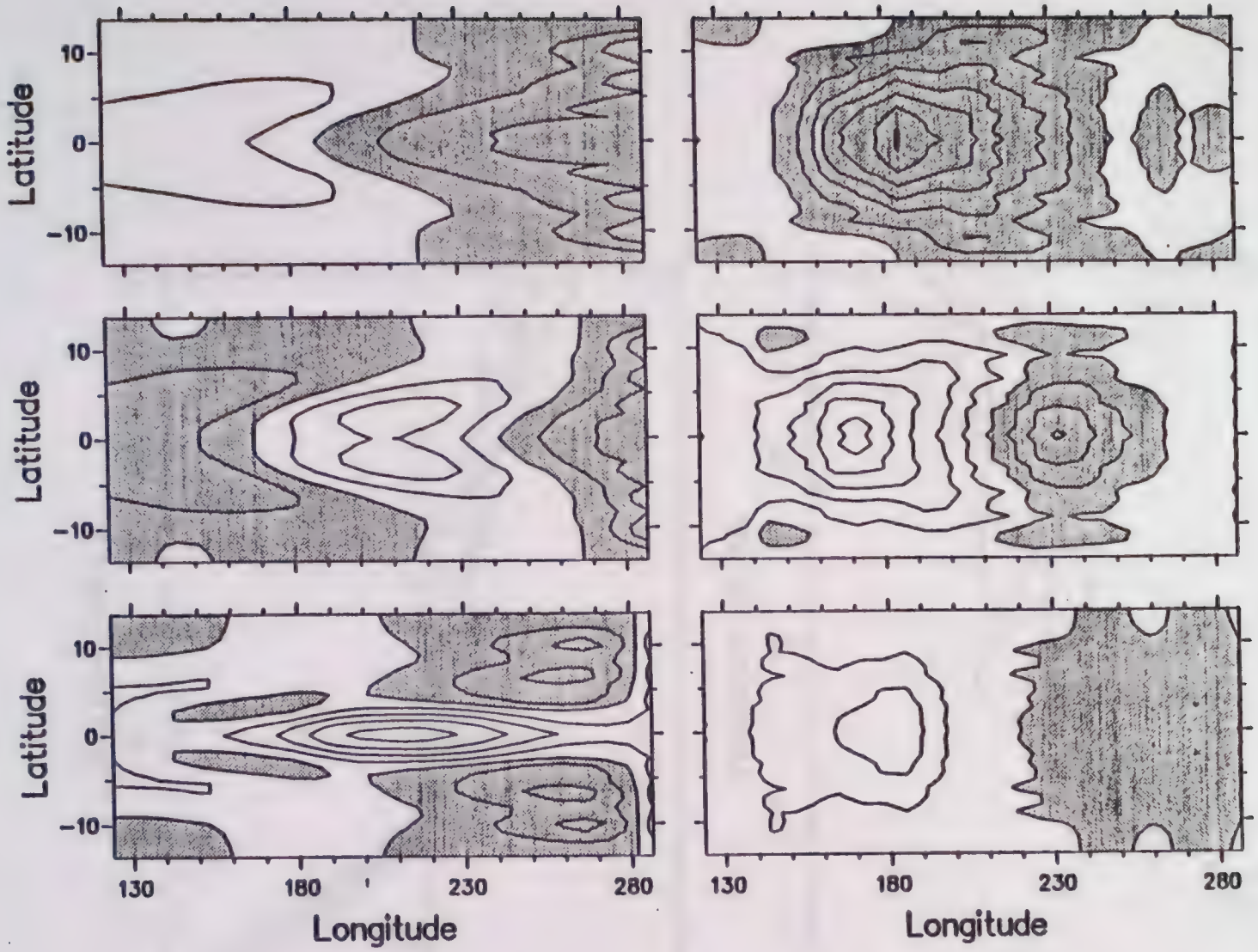

Fig. 11: The first (top), second (middle), and third (bottom) EOF patterns of model ocean layer depth anomalies (left), and associated zonal wind stress anomalies (right). Contour intervals are arbitrary, negative values are shaded.

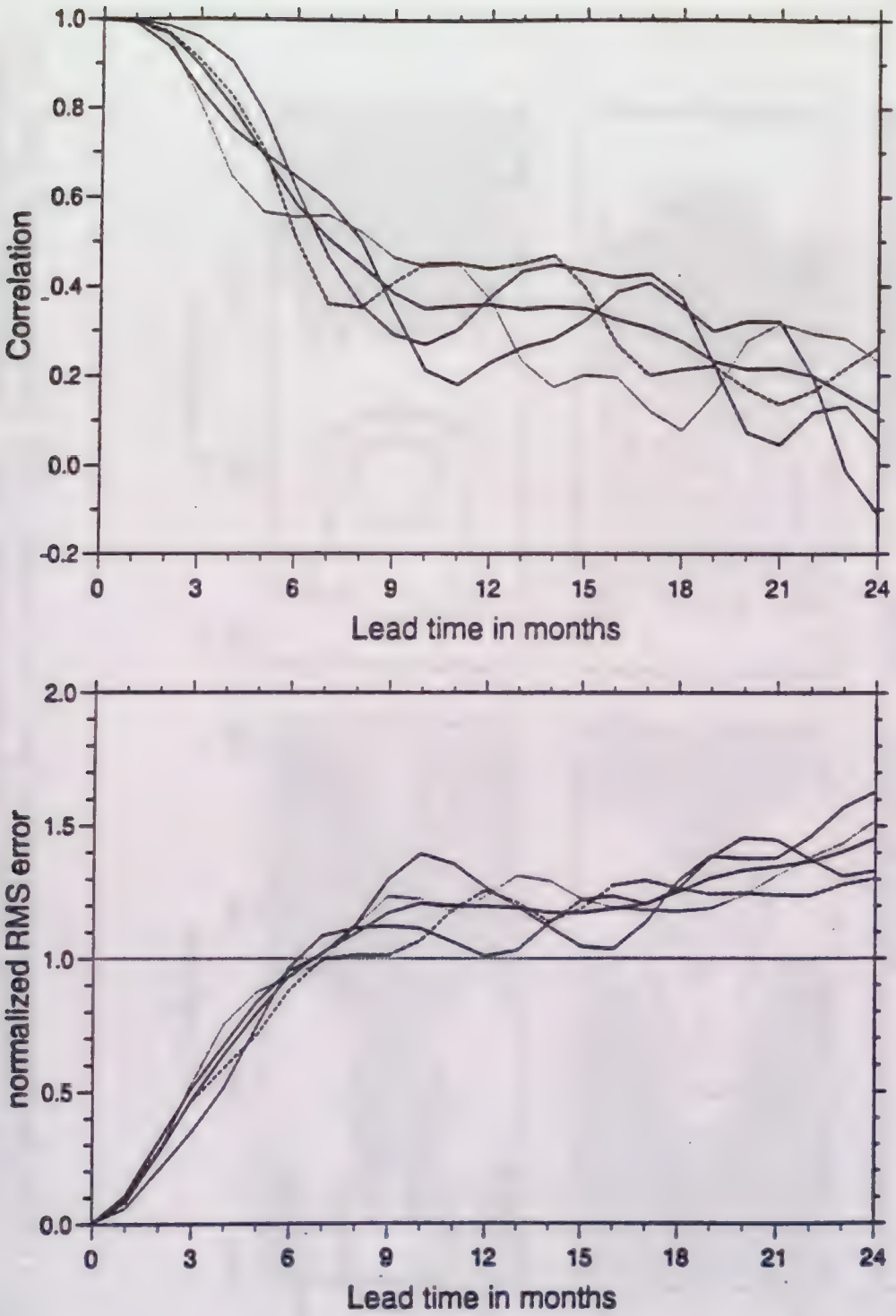

Fig. 12a: Correlations between predictions and control values of SST anomalies in the Niño3 region as a function of lead time (top), and corresponding rms error (bottom) normalised by the standard deviation of the control run. Solid lines are for the full dataset (using 100 predictions), while broken lines are for predictions grouped according to start month: January (long dash), April (dot), July (fine dash), October (dash-dot)

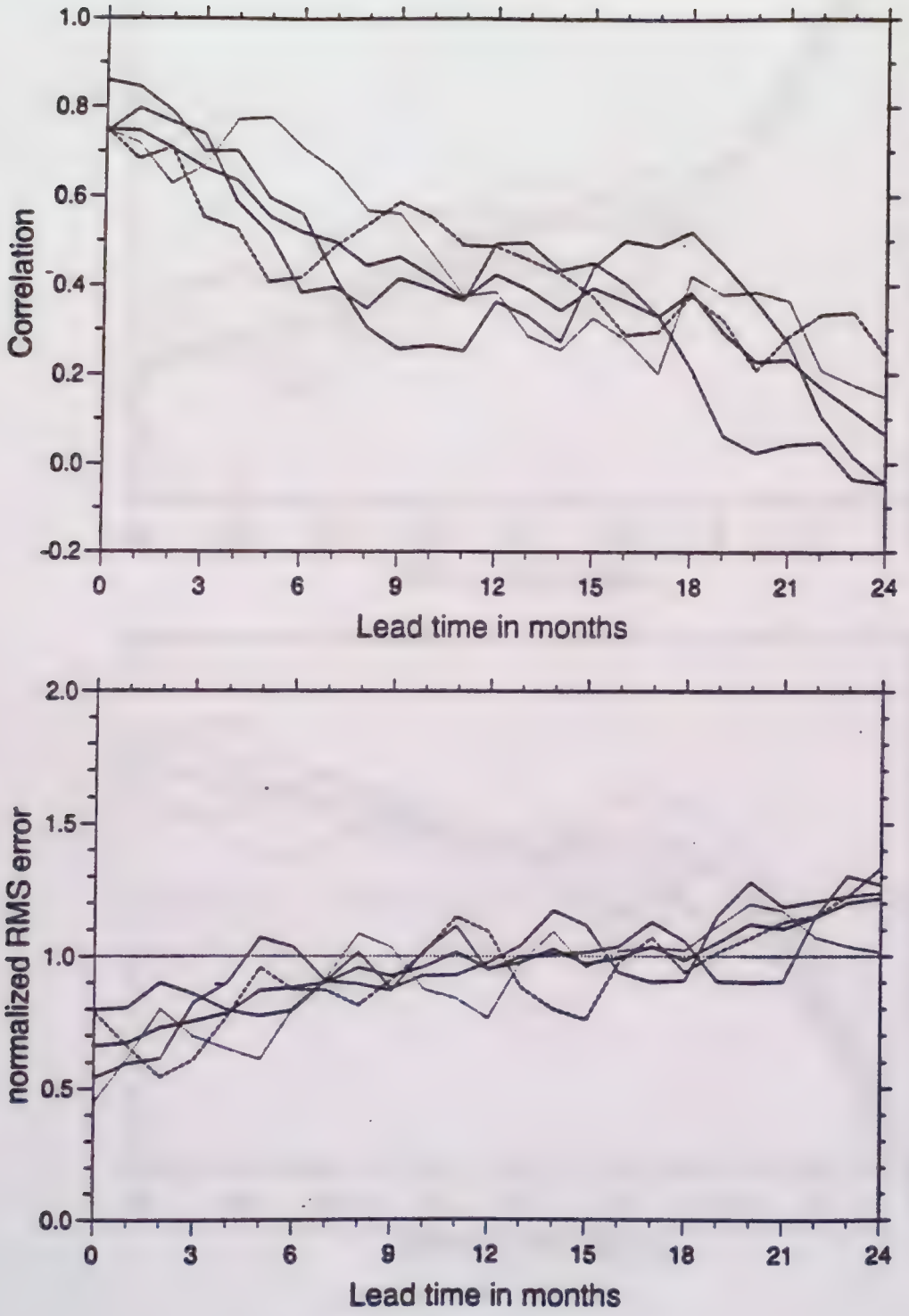

Fig. 12b: Correlations between predictions and observed values of SST anomalies in the Niño3 region as a function of lead time (top), and corresponding rms error (bottom) normalised by the standard deviation of observations. Solid lines are for the full dataset (using 100 predictions), while broken lines are for predictions grouped according to start month: January (long dash), April (dot), July (fine dash), October (dash-dot)

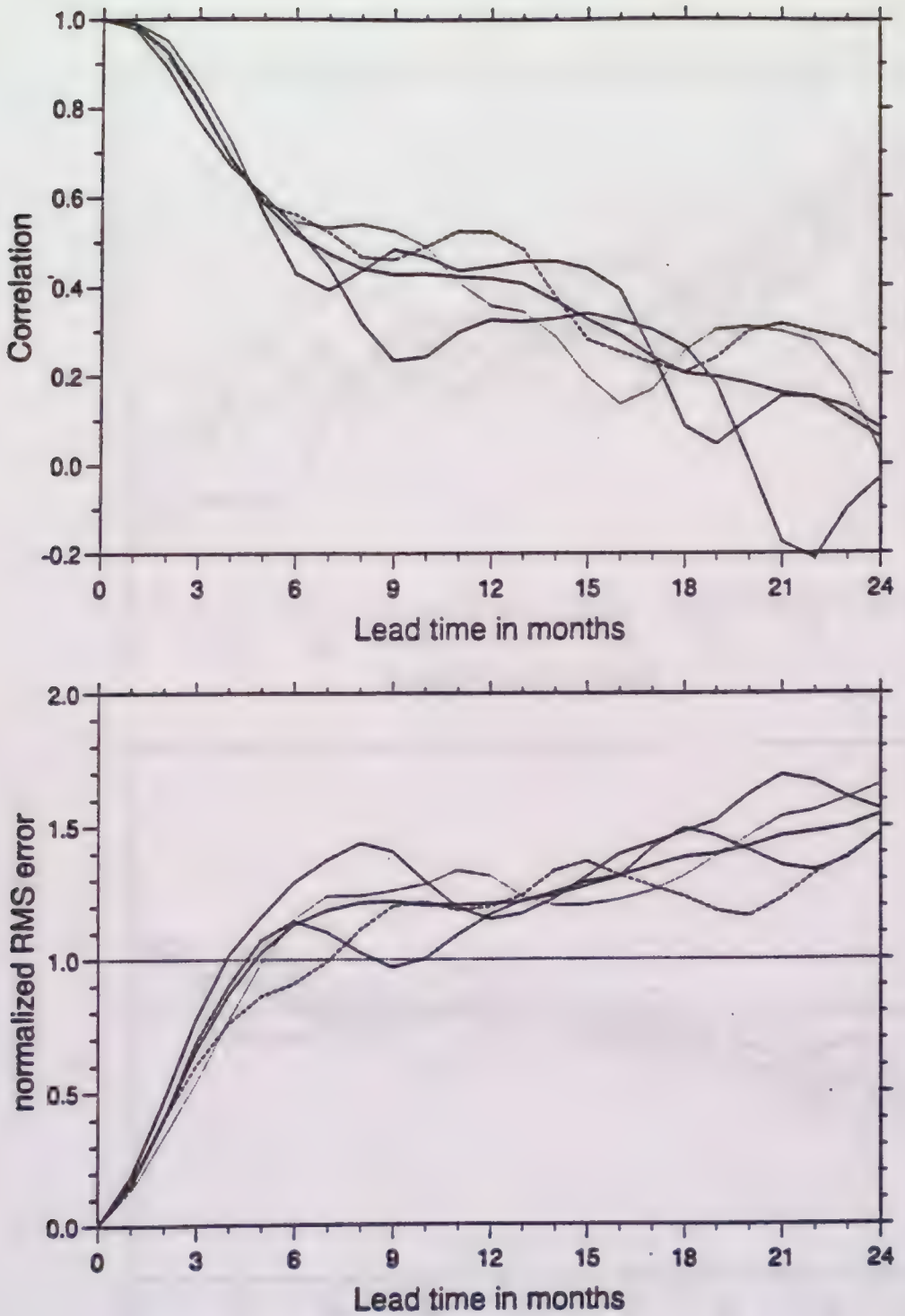

Fig. 13a: Correlations between predictions and control values of SST anomalies in the Niño4 region as a function of lead time (top), and corresponding rms error (bottom) normalised by the standard deviation of the control run. Solid lines are for the full dataset (using 100 predictions), while broken lines are for predictions grouped according to start month: January (long dash), April (dot), July (fine dash), October (dash-dot)

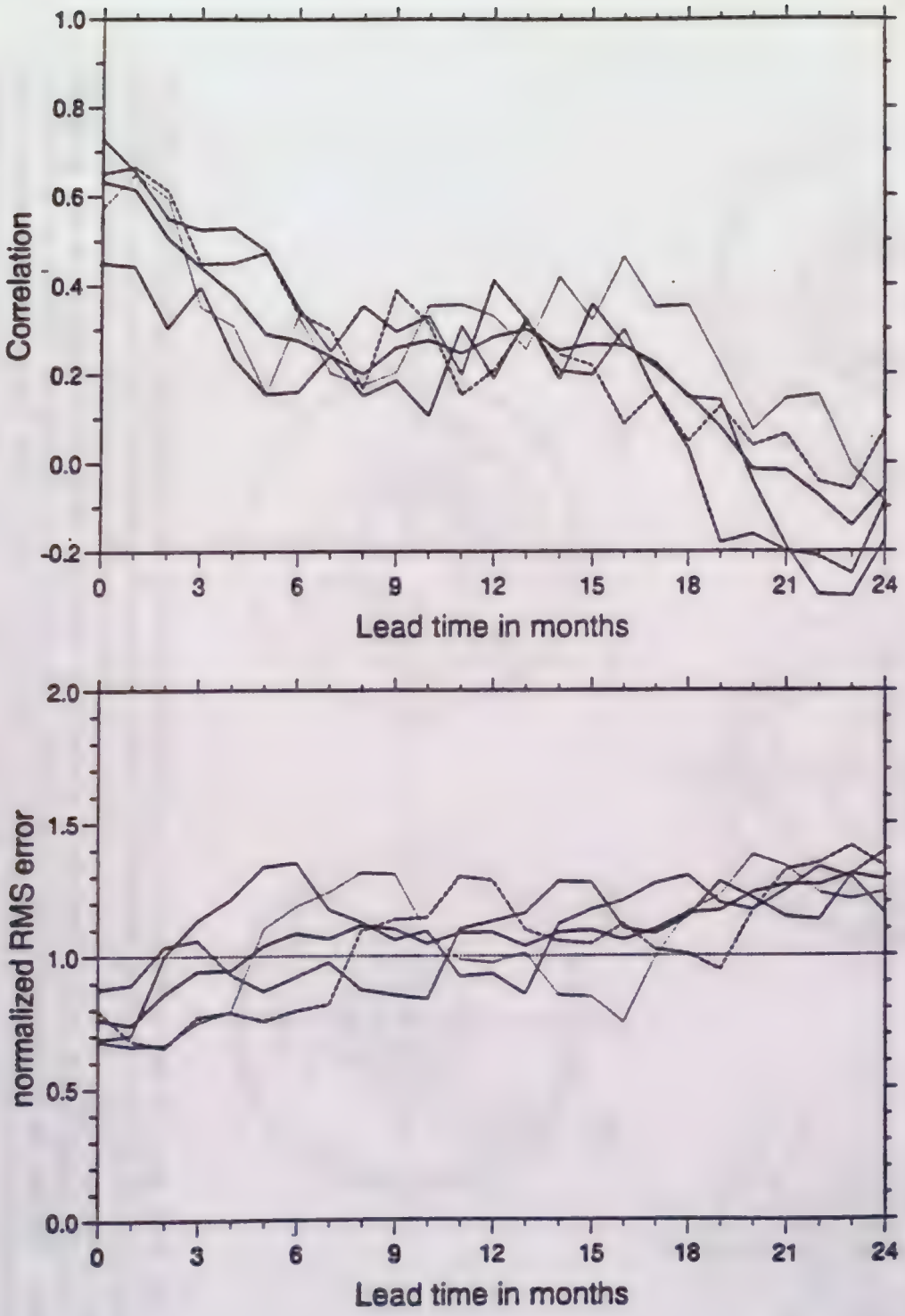

Fig. 13b: Correlations between predictions and observed values of SST anomalies in the Niño4 region as a function of lead time (top), and corresponding rms error (bottom) normalised by the standard deviation of observations. Solid lines are for the full dataset (using 100 predictions), while broken lines are for predictions grouped according to start month: January (long dash), April (dot), July (fine dash), October (dash-dot)

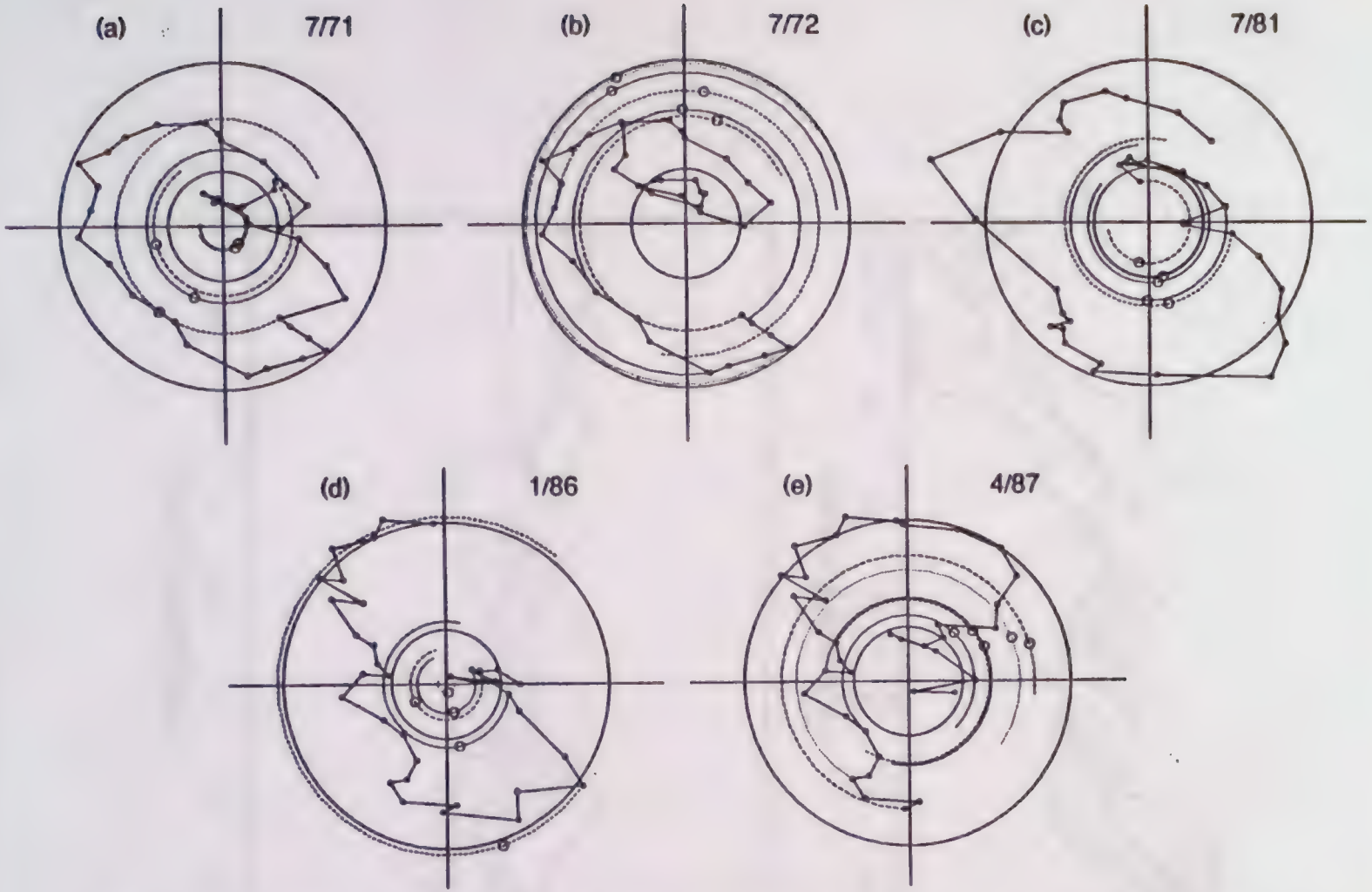

Fig. 14: Dial plots of the coefficients of real (horizontal axis) and imaginary (vertical axis) principal oscillation patterns for the dominant ENSO POP mode. Values are scaled such that the maximum absolute value is 1; reference rings in each diagram indicate amplitudes of 0.25 and 0.75 . The solid curves are values from the control run, with black dots at monthly intervals (note that trajectories are generally clockwise). Broken lines show predicted trajectories, starting at control values. (Decay is omitted, so predicted amplitude is constant: predicted period is that of the ENSO POP mode.) The number at top-right of each diagram is the starting time of the first prediction: others follow at three month intervals. Open circles on the prediction trajectories mark the time when the corresponding control run reached peak phase (i.e. when the control real coefficient is closest to zero - see text for details.)

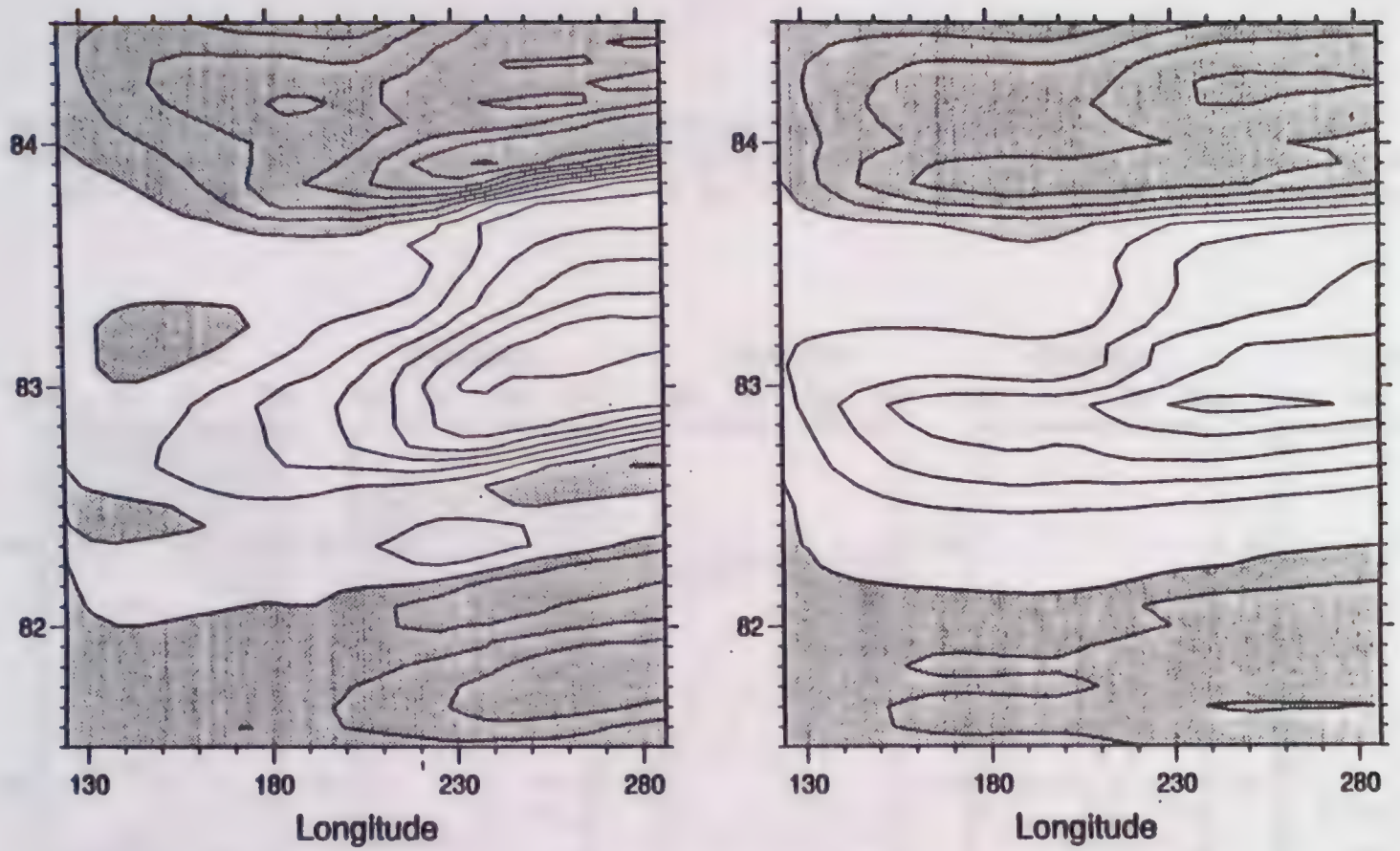

Fig. 15a: SST anomalies along the equator for the 82/83 event from the control run (left) and as reconstructed by the ENSO POP mode with coefficients from the control run (see Fig. 14c). Contour interval 0.5°C, negative values shaded.

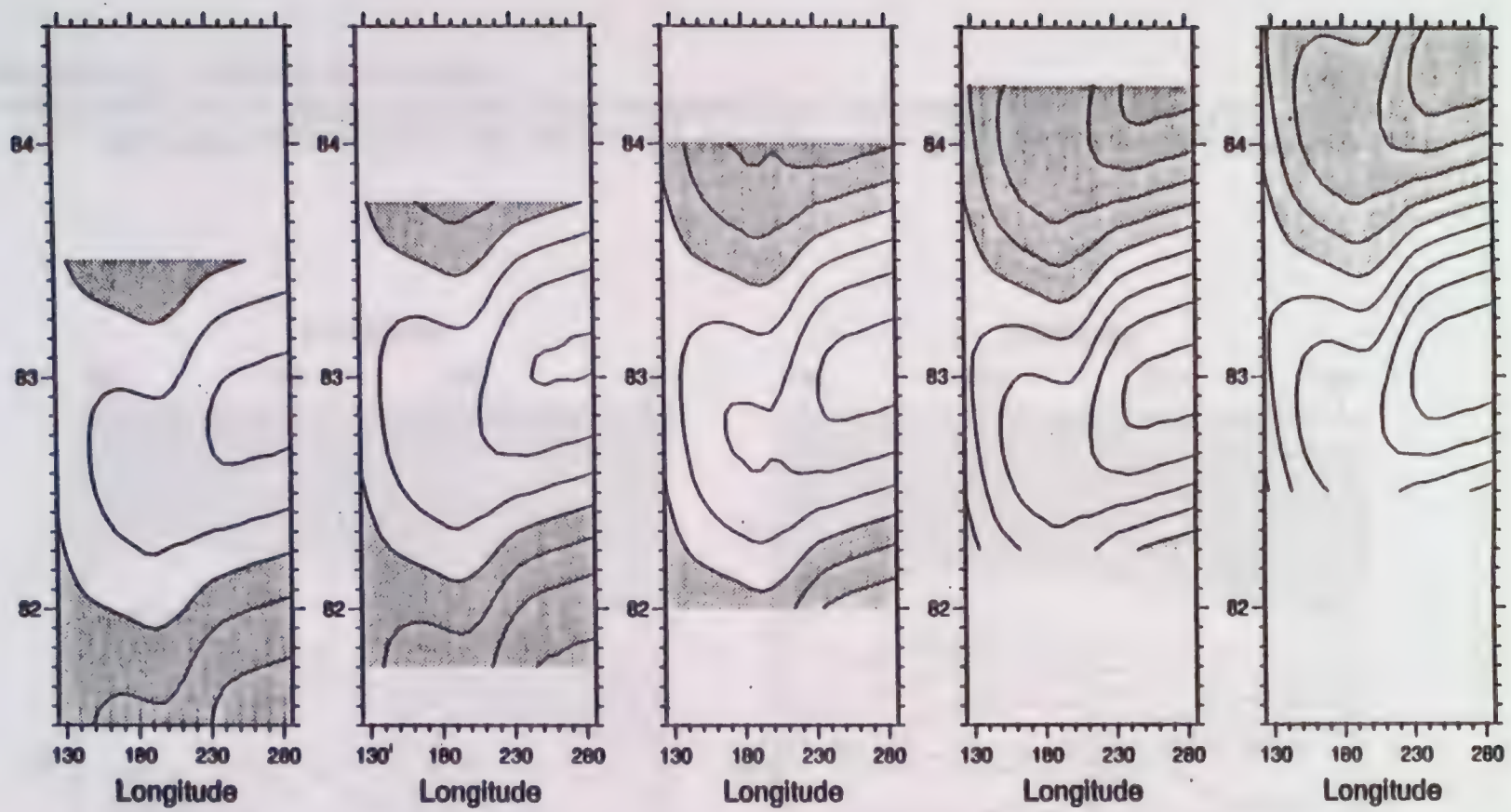

Fig. 15b: Patterns of SST anomalies along the equator for the 82/83 event as realised by 5 POP predictions (see Fig. 14c). Negative values are shaded. Here contour intervals are arbitrary, but scaled such that intercomparison of the predicted patterns can be made readily.

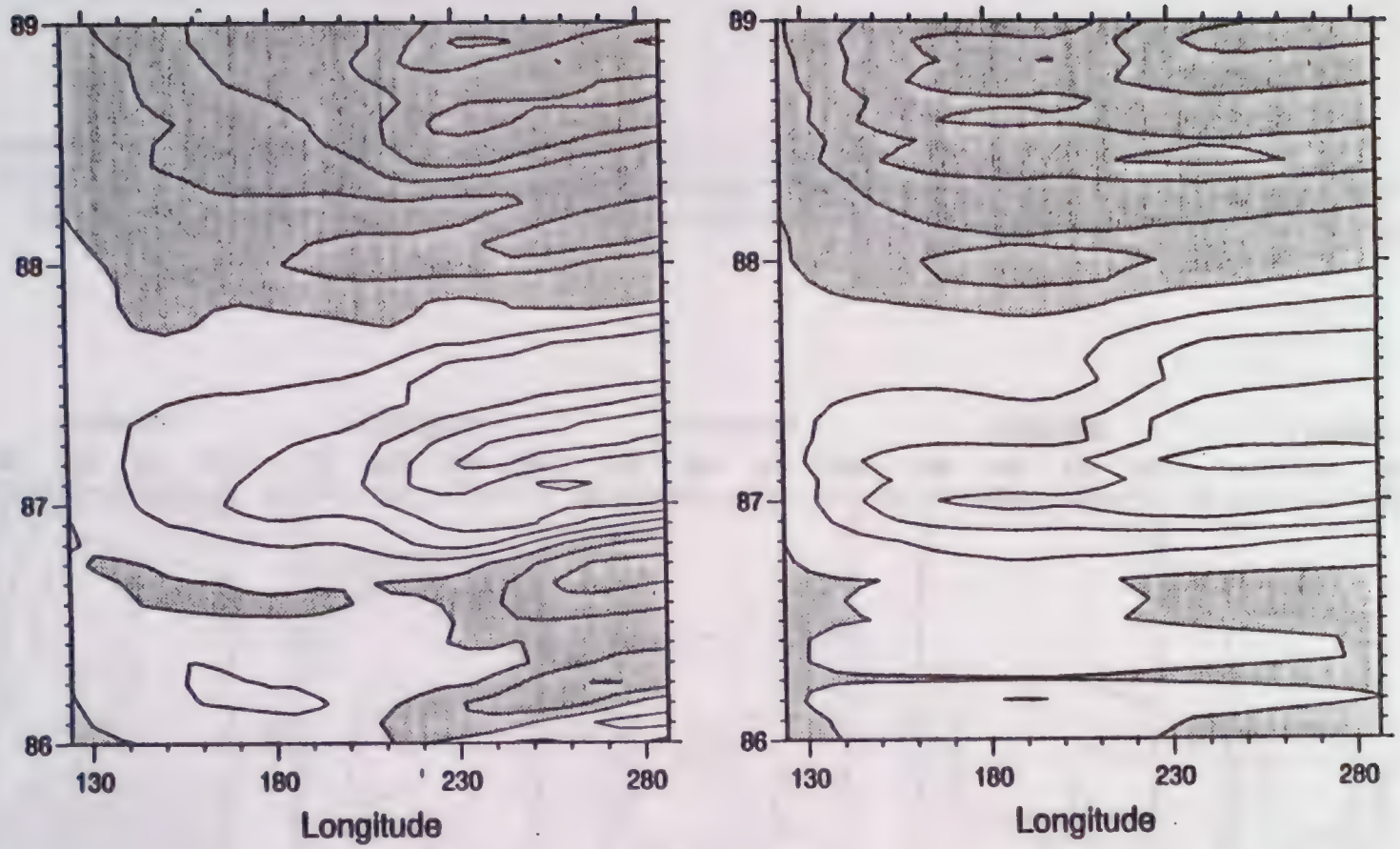

Fig. 16a: SST anomalies along the equator for the 86/87 event from the control run (left) and as reconstructed by the ENSO POP mode with coefficients from the control run (see Fig. 14d). Contour interval 0.5°C, negative values shaded.

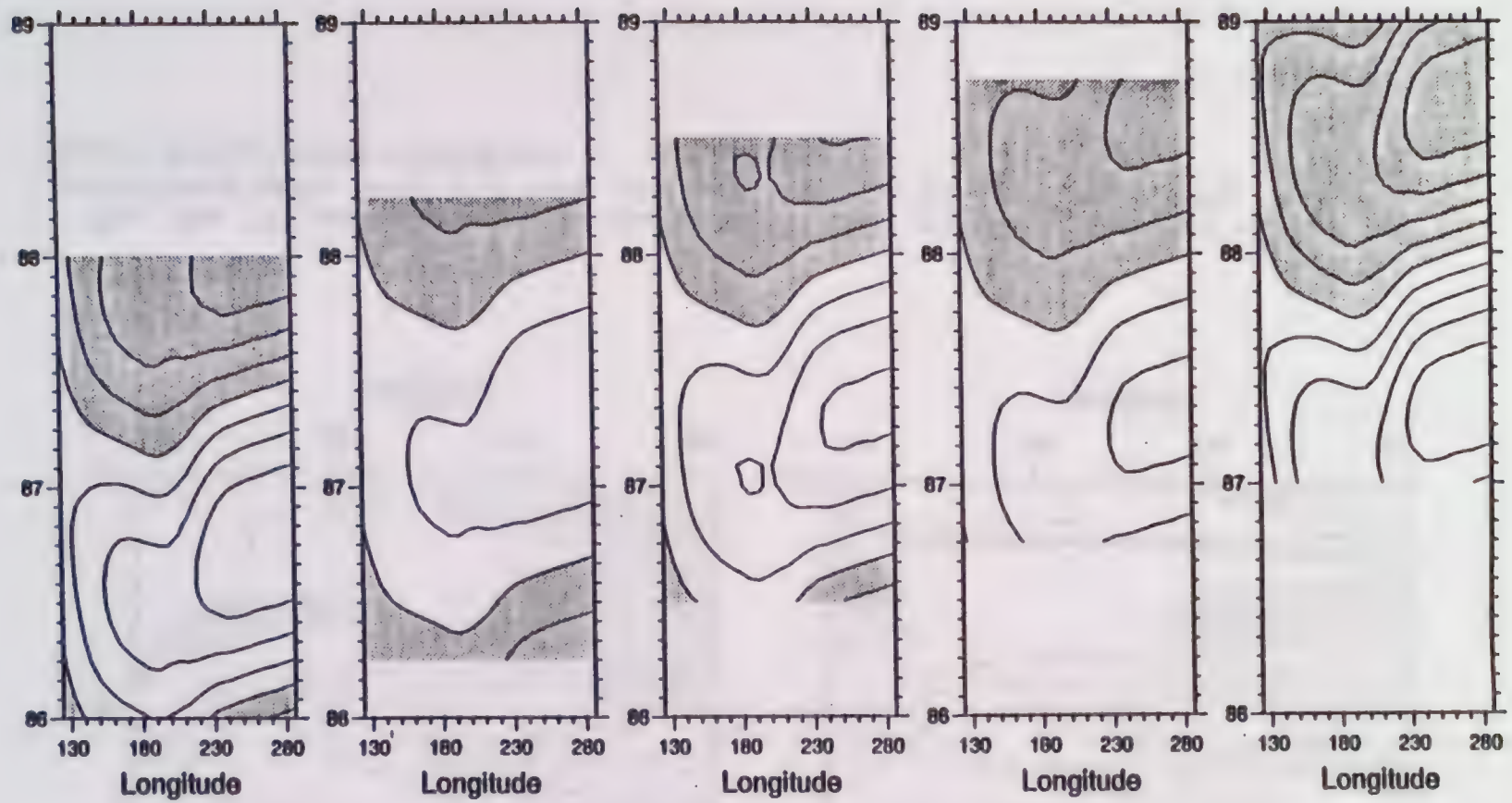

Fig. 16b: Patterns of SST anomalies along the equator for the 86/87 warm event as realised by 5 POP predictions (see Fig. 14d). Negative values are shaded. Differing contour intervals are used for ease of comparison: multiplying factors are (a) 2, (b) 1, (c) 2, (d) 6, (e) 8.

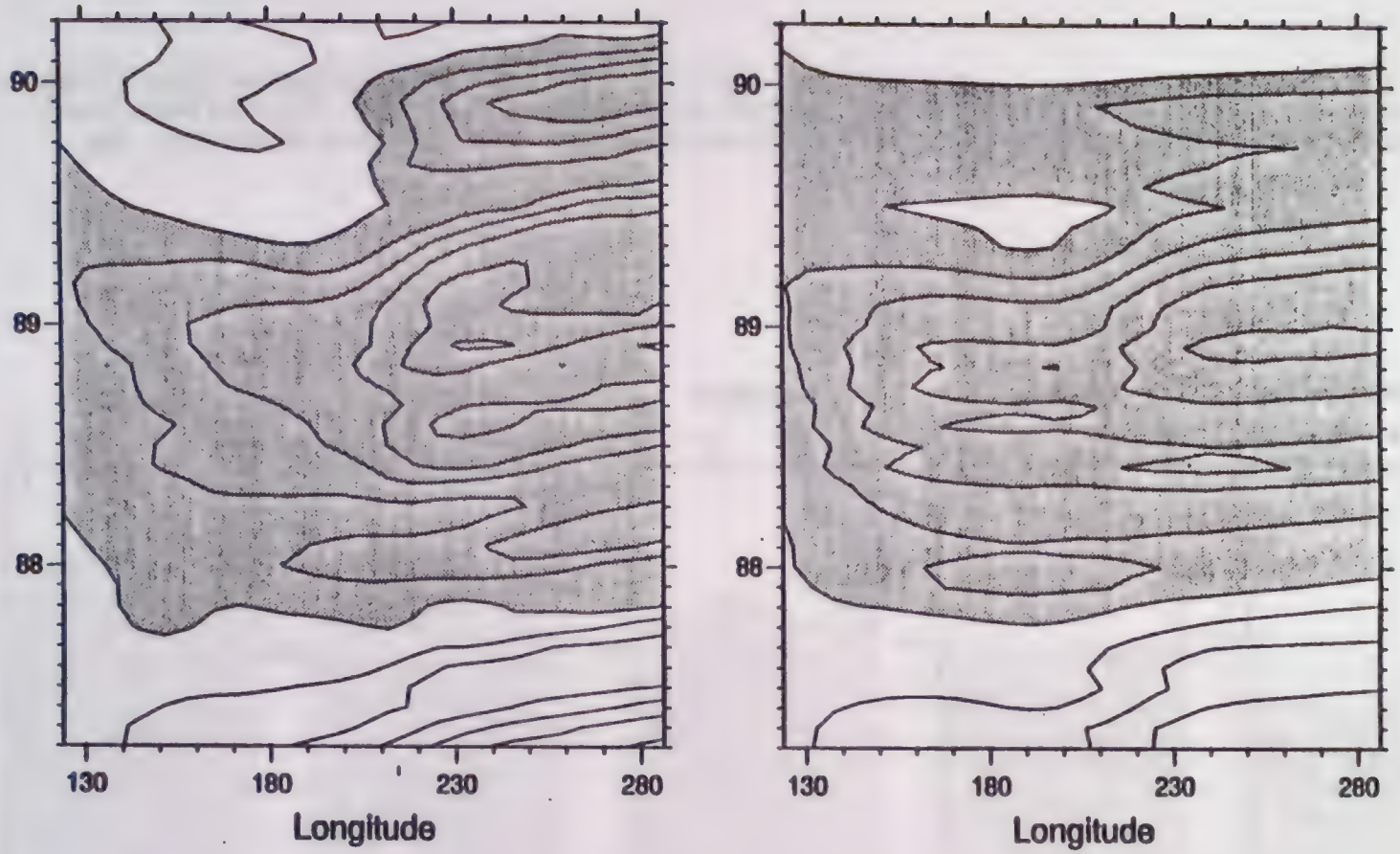

Fig. 17a: SST anomalies along the equator for the 87/88 cold event from the control run (left) and as reconstructed by the ENSO POP mode with coefficients from the control run (see Fig. 14d). Contour interval 0.5°C, negative values shaded.

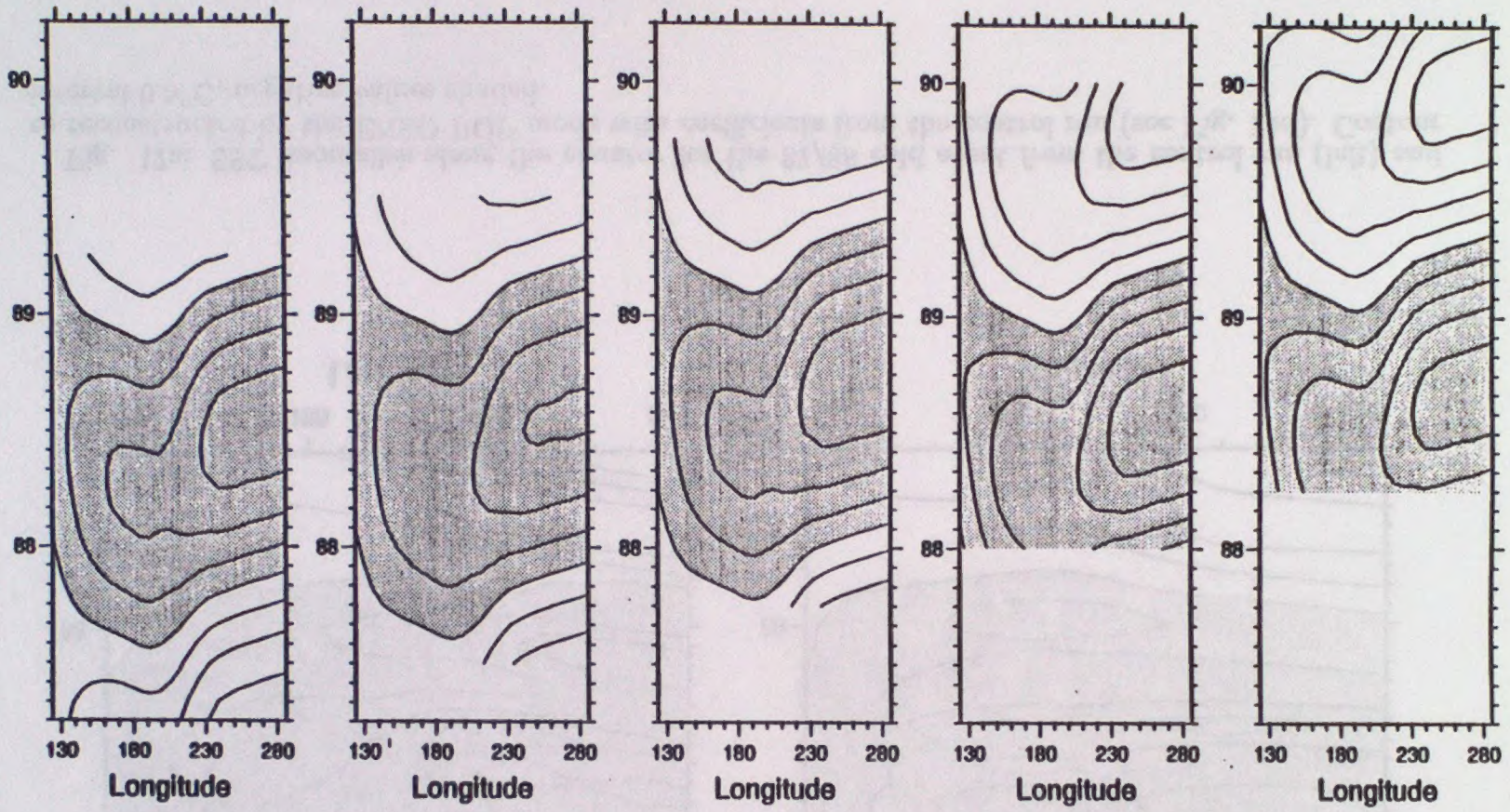

Fig. 17b: Patterns of SST anomalies along the equator for the 87/88 cold event as realised by 5 POP predictions (see Fig. 14d). Negative values are shaded. Differing contour intervals are used for ease of comparison: multiplying factors are (a) 2, (b) 2, (c) 1, (d) 1, (e) 1.

CLIMATE RESEARCH TECHNICAL NOTES

CRTN 1	Oct 1990	Estimates of the sensitivity of climate to vegetation changes using the Penman-Monteith equation. P R Rowntree
CRTN 2	Oct 1990	An ocean general circulation model of the Indian Ocean for hindcasting studies. D J Carrington
CRTN 3	Oct 1990	Simulation of the tropical diurnal cycle in a climate model. D P Rowell
CRTN 4	Oct 1990	Low frequency variability of the oceans. C K Folland, A Colman, D E Parker and A Bevan
CRTN 5	Dec 1990	A comparison of 11-level General Circulation Model Simulations with observations in the East Sahel. K Maskell
CRTN 6	Dec 1990	Climate Change Prediction. J F B Mitchell and Qing-cun Zeng
CRTN 7	Jan 1991	Deforestation of Amazonia - modelling the effects of albedo change. M F Mylne and P R Rowntree
CRTN 8	Jan 1991	The role of observations in climate prediction and research. D J Carson
CRTN 9	Mar 1991	The greenhouse effect and its likely consequences for climate change. D J Carson
CRTN 10	Apr 1991	Use of wind stresses from operational N.W.P. models to force an O.G.C.M. of the Indian Ocean. D J Carrington
CRTN 11	Jun 1991	A new daily Central England Temperature series, 1772-1991. D E Parker, T P Legg and C K Folland
CRTN 12	Jul 1991	Causes and predictability of Sahel rainfall variability. D P Rowell, C K Folland, K Maskell, J A Owen, M N Ward
CRTN 13	Jul 1991	Modelling changes in climate due to enhanced CO_2, the role of atmospheric dynamics, cloud and moisture. C A Senior, J F B Mitchell, H Le Treut and Z-X Li

CLIMATE RESEARCH TECHNICAL NOTES

CRTN 14	Sep 1991	Sea temperature bucket models used to correct historical SST data in the Meteorological Office. C K Folland
CRTN 15	Aug 1991	Modelling climate change, and some potential effects on agriculture in the U.K. P R Rowntree, B A Callander and J Cochrane
CRTN 16	Aug 1991	The Boreal Forests and Climate G Thomas and P R Rowntree
CRTN 17	Aug 1991	Development of a Stratosphere-Troposphere Data Assimilation System. R Swinbank.
CRTN 18	Sep 1991	A study of asynchronous coupling using a simple climate model. M K Davey.
CRTN 19	Sep 1991	The Oceanic Carbon Cycle. N K Taylor
CRTN 20	Nov 1991	Worldwide ocean-atmosphere surface fields in Sahel wet and dry years using provisionally corrected surface wind data. M N Ward
CRTN 21	Dec 1991	Coupled tropical ocean global atmosphere models at the UKMO. M K Davey, C Gordon, S Ineson and S Lawrence
CRTN 22	Dec 1991	Empirical parameterisation of tropical ocean-atmosphere coupling. M Allen, M K Davey, D L T Anderson and P D Killworth
CRTN 23	Feb 1992	The temporal evolution of Equatorial Currents in the Indian Ocean D L T Anderson, D J Carrington, R A Corry and C Gordon
CRTN 24	Feb 1992	Stratospheric analyses provided by the U.K. Meteorological Office M J Bailey, A O'Neill and V D Pope
CRTN 25	Feb 1992	Modelling interannual variability in the Indian Ocean using momentum fluxes from the UKMO and ECMWF operational weather analyses. D L T Anderson and D J Carrington

CLIMATE RESEARCH TECHNICAL NOTES

CRTN 26	Mar 1992	A GCM simulation of the impact of Amazonian deforestation on climate using an improved canopy representation J Lean and P R Rowntree
CRTN 27	Mar 1992	The parameterization of rainfall interception in GCMs A J Dolman and D Gregory
CRTN 28	Jun 1992	Development of worldwide marine data eigenvectors since 1985 A W Colman
CRTN 29	Jun 1992	A tropical ocean model with reduced physics M K Davey
CRTN 30	Jun 1992	International Temperature Workshop, Boulder, Colorado, USA, 16 January 1992 Edited by D E Parker
CRTN 31	Jul 1992	Simulation of clear-sky outgoing longwave radiation over the oceans using operational analyses A Slingo and M J Webb
CRTN 32	Sep 1992	A prediction of the transient response of climate J M Murphy
CRTN 33	Nov 1992	LEPS scores for assessing climate model simulations and long-range forecasts. C K Folland
CRTN 34	Jan 1993	Stratospheric Data Assimilation System Guide Editer: R Swinbank
CRTN 35	Mar 1993	A Stratosphere-Troposphere Data Assimilation System R Swinbank and A O'Neill
CRTN 36	Mar 1993	Validation of hydrological schemes for climate models against catchment data. P R Rowntree and J Lean
CRTN 37	Apr 1993	Modelling of palaeoclimates: Examples from the recent past J F B Mitchell
CRTN 38	May 1993	A simulation of seasonality in ENSO forecast skill M K Davey, D L T Anderson and S Lawrence
CRTN 39	Jul 1993	ENSO Prediction experiments using a simple ocean-atmosphere model D-H Wu, D L T Anderson and M K Davey